
Inspiring the Next Generation of Segment Anything Models: Comprehensively Evaluate SAM and SAM 2 with Diverse Prompts Towards Context-Dependent Concepts under Different Scenes

Xiaoqi Zhao^{1,2*} Youwei Pang^{1*} Shijie Chang^{1*} Yuan Zhao^{1*}
Lihe Zhang¹ Huchuan Lu¹ Georges El Fakhri² Xiaofeng Liu²
¹Dalian University of Technology ²Yale University
{zxq, lartpang}@gmail.com
<https://github.com/lartpang/SAMs-CDConcepts-Eval>

Abstract

As a foundational model, SAM has significantly influenced multiple fields within computer vision, and its upgraded version, SAM 2, enhances capabilities in video segmentation, poised to make a substantial impact once again. While SAMs (SAM and SAM 2) have demonstrated excellent performance in segmenting context-independent concepts like people, cars, and roads, they overlook more challenging context-dependent (CD) concepts, such as visual saliency, camouflage, product defects, and medical lesions. CD concepts rely heavily on global and local contextual information, making them susceptible to shifts in different contexts, which requires strong discriminative capabilities from the model. The lack of comprehensive evaluation of SAMs limits understanding of their performance boundaries, which may hinder the design of future models. In this paper, we conduct a thorough quantitative evaluation of SAMs on 11 CD concepts across 2D and 3D images and videos in various visual modalities within natural, medical, and industrial scenes. We develop a unified evaluation framework for SAM and SAM 2 that supports manual, automatic, and intermediate self-prompting, aided by our specific prompt generation and interaction strategies. We further explore the potential of SAM 2 for in-context learning and introduce prompt robustness testing to simulate real-world imperfect prompts. Finally, we analyze the benefits and limitations of SAMs in understanding CD concepts and discuss their future development in segmentation tasks. This work aims to provide valuable insights to guide future research in both context-independent and context-dependent concepts segmentation, potentially informing the development of the next version — SAM 3.

1 Introduction

As a foundation model in the field of image segmentation, Segment Anything Model (SAM [37]) has demonstrated remarkable performance across various scenarios, spurring research interest in unified/generalist models [96, 79, 52], in-context visual learning [80, 6, 47], and SAM-adaptors [35, 83, 78]. Recently, the upgraded version, SAM 2 [59], has introduced powerful video object segmentation capabilities, expected to ignite a new wave of research.

In philosophy and cognitive science [2], the concept of an object is typically divided into context-independent (CI) and context-dependent (CD) concepts. Recently, Zhao *et al.* [96] first provide a

*Equal contribution.

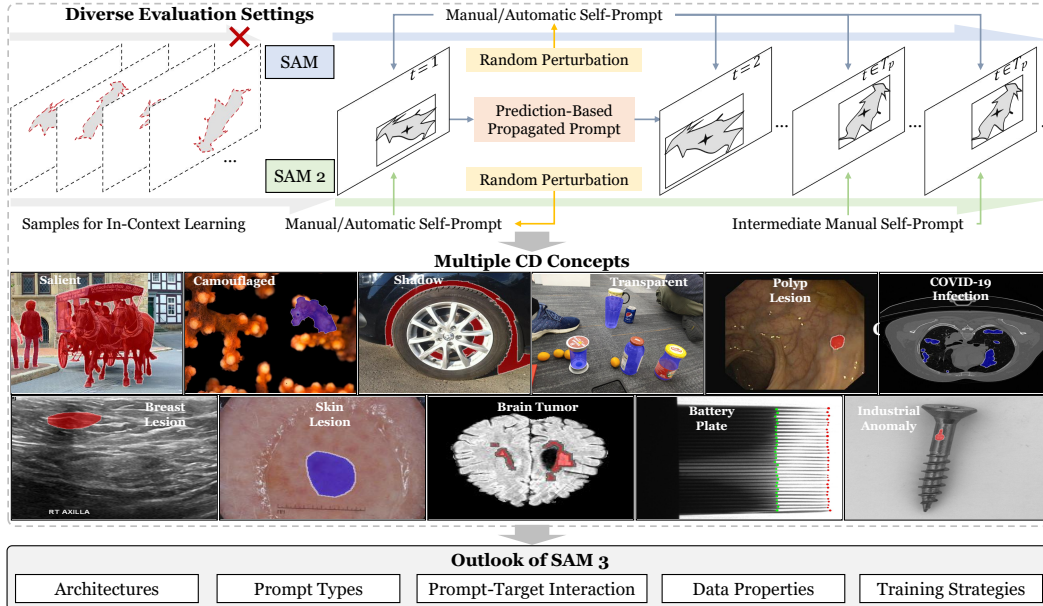


Figure 1: Organization. (1) A unified evaluation framework for SAM and SAM 2; (2) Comprehensive evaluation for 11 different context-dependent concepts; (3) Outlook of SAM 3.

Table 1: Summary of the characteristics in different evaluation works. Different prompt types: \square : Everything; \star : Mask; \square : Box; \odot : Point; \diamond : In-Context Learning. “+PR”: Prompt Robustness Analysis.

Method	Scene	CD Concept	Datasets	Modality	Prompt Modes
Ji <i>et al.</i> [33]	Natural	Camouflaged Object	CAMO [39], COD10K [22], NC4K [51], CHAMELEON [67]	RGB Image	\square
Ji <i>et al.</i> [34]	Natural	Salient Object	DUTS [77], COME15K-Diff [91], VT1000 [72], DIS-TE4 [58]	RGB Image	\square
		Camouflaged Object	COD10K [22], CDS2K [23]	RGB Image	\square
		Shadow Object	SBU [75]	RGB Image	\square
		Polyp Lesion	CVC-ColonDB [69]	Endoscopy	\square
Zhou <i>et al.</i> [99]	Medical	Polyp Lesion	Kvasir [31], ETIS [66], CVC-ClinicDB [4], CVC-ColonDB [69], Endoscene [73]	Endoscopy	\square
Tang and Li [71]	Natural	Camouflaged Object	CAMO [39], COD10K [22], NC4K [51], MoCA-Mask [38]	RGB Image RGB Video	\square , \square , \odot
Lian and Li [42]	Natural	Salient Object	USIS10K [43]	RGB Image	\square , \square , \odot
Chen <i>et al.</i> [11]	Natural	Camouflaged Object	CHAMELEON [67], CAMO [39], COD10K [22]	RGB Image	\square
		Shadow Object	ISTD [76]	RGB Image	\square
		Polyp Lesion	Kvasir [31]	Endoscopy	\square
Ours	Natural	Salient Object	DUTS [77], ECSSD [87], DUT-OMRON [88], HKU-IS [40], PASCAL-S [41], DAVIS-16 [57], DAVSOD [25]	RGB Image RGB Video	\square , \square , \odot , \star , \diamond , +PR \square , \square , \odot , \star , \diamond , +PR
		Camouflaged Object	CAMO [39], COD10K [22], NC4K [51], CAD [5], MoCA-Mask [14]	RGB Image RGB Video	\square , \square , \odot , \star , \diamond
		Shadow Object	SBU [75], ISTD [76], VISAD-DS [48], VISAD-MOS [48]	RGB Image RGB Video	\square , \square , \odot , \star , \diamond
		Transparent Object	Trans10K [85]	RGB Image	\square , \square , \odot , \star , \diamond
		Polyp Lesion	Kvasir [31], ETIS [66], CVC-ClinicDB [4], CVC-ColonDB [69], Endoscece [73], CVC-612-T [32], CVC-612-V [32], CVC-300-TV [32]	Endoscopy Image Endoscopy Video	\square , \square , \odot , \star , \diamond
	Medical	Skin Lesion	ISIC-2018 [16]	Dermoscopy	\square , \square , \odot , \star , \diamond
		Lung Infection	COVID-19 CT [26]	CT	\square , \square , \odot , \star , \diamond
		Brain Tumor	BraTS2020 [54], ISBI2015 [8]	MRI (T1/T2/T1ce/Flair)	\square , \square , \odot
		Breast Lesion	BUSI [1]	Ultrasound	\square , \square , \odot , \star , \diamond
		Power Battery Plate	PBD [95] (Regular/Difficult/Tough)	X-ray	\square , \square , \odot
	Industrial	Surface Anomaly	MVTec-AD [3], VisA [100], BTAD [55]	RGB Image	\square , \square , \odot , +PR

detailed distinction of CI and CD concepts within the image segmentation field. Traditional semantic segmentation datasets [7, 18] usually focus on the CI concepts such as roads, vehicles, and people that are relatively easy to segment. Regardless of the environment, the shape and category of these objects are stable, allowing models to focus solely on the intrinsic features of the objects for effective segmentation. In real-world scenarios, predictions of CI concepts often serve as preliminary steps for further scene analysis. Different from them, CD concept segmentation tasks are explicitly oriented towards functional applications, demonstrating direct value in visual attention perception, medical

lesion segmentation, and industrial inspection. However, due to the environmental dependence, concept variability, and scene specificity, existing CD concepts methods often rely on domain-specific specialized models, making unified CD concept segmentation more challenging. Can SAMs perfectly segment CD concepts? Existing works have evaluated the segmentation performance of SAMs on saliency [42], camouflage [33], shadow [11], and colon polyps [99]. As shown in Tab. 1, these evaluations are too domain-specific rather than the high-level CD concepts perspective. Most of these studies are limited to quantitative evaluations on a small set of datasets under the everything prompt mode. Compared with them, we have obvious advantages in the evaluation breadth and depth of scenarios, CD concepts, datasets, modalities, and prompting types. We believe that to fairly assess the capability of SAMs in CD concepts segmentation, it is essential to conduct enough experiments on diverse concepts and benchmarks, as well as a variety of prompt types and strategies. Insufficient experimentation can easily introduce bias and lead to subjective conclusions.

The organization and contributions of this paper are illustrated in Fig. 1. **First**, we design a unified evaluation framework for SAMs, integrating manual, automatic, and intermediate manual self-prompting methods. Everything, point, and box prompts naturally fall within this comprehensive scope. Notably, we develop a prediction-based propagated prompt and non-current sample prompting for in-context learning inference mode, targeting the serialization predictions and memory attention characteristics of SAM 2. **Next**, we conduct quantitative experiments on image segmentation in both basic and in-context learning modes, as well as video and 3D segmentation across 33 datasets covering 11 CD concepts. **Finally**, we conduct an in-depth analysis of current representative unified segmentation models in terms of architecture, prompt types, prompt-target interactions, training data, and strategies to inspire the next generation of Segment Anything Models.

2 Related Works

2.1 Context-Dependent Concepts Segmentation

Context-dependent (CD) concept segmentation has garnered significant attention over the years. These concepts rely on specific spatial contexts to define the concepts of interest, posing unique challenges and driving advanced designs for specialized models. **I) Background Complexity and Similarity.** In tasks like camouflaged and transparent object segmentation, highly similar backgrounds make it difficult for the model to distinguish between the target object and surroundings. This requires models with enhanced background understanding and segmentation capabilities [21, 56, 63]. **II) Object Boundary Ambiguity.** In tasks such as transparent object and medical lesion segmentation, smooth transitions between the object and surroundings often lead to boundary ambiguity. Models can missegment these fuzzy edges, necessitating precise boundary recognition and shape modeling capabilities [24, 98, 9]. **III) Context Dependency.** Models need strong context-awareness, adjusting segmentation strategies based on the surrounding environment rather than relying solely on local features of the target objects [44, 17, 12].

2.2 Unified Multi-Concept Segmentors

The development of large foundation models and visual prompt technology has led to the emergence of various models aimed at achieving AGI, notably in unified and generalist segmentation. Over the past year, SAM has become a standout segmentor due to its simple architecture, extensive data training, and impressive performance. Following SAM, more generalist models aim to accurately segment context-independent concepts with different prompt learning strategies. UniverSeg [6] excels in unifying medical image segmentation across diverse tasks with domain-agnostic representations. SegGPT [80] employs flexible, prompt-based segmentation using transformer architecture, while HQSAM [35] produces high-quality, high-resolution masks with strong generalization and real-time inference. For context-dependent concepts, EVP [46] enhances low-level structure segmentation through explicit visual prompting, while GateNetv2 [97] offers a versatile gated network for various CD concepts tasks. Spider [96] and VSCoDe [50] leverage 2D prompt learning to understand background-foreground relationships. Recently, SAM 2 built on SAM by introducing memory attention and multiple frame prompts, utilizing large video datasets to advance video object segmentation. Its approach is expected to invigorate 3D, video, and few-shot/co-segmentation fields.

2.3 SAMs Evaluation

The development of any technology inherently presents a dual nature. On one hand, SAMs, as segmentation foundation models, provide significant potential for direct application across tasks. On the other hand, SAMs challenge the long-standing independence of specialized segmentation sub-fields, raising the question, “Is segmentation as we know it obsolete?” Existing reports have focused on tasks like camouflaged object detection (COD) [33], shadow detection [34], polyp segmentation [99], and underwater salient object detection [42]. Following the trend in unified/specialist segmentation methods, which categorizes segmentation into context-independent (CI) and context-dependent (CD) concepts, we aim to provide a fair and comprehensive evaluation of SAMs’ performance across various CD concepts. The goal is to establish an evaluation baseline for future research, minimizing redundant work.

3 Experiments

3.1 Datasets and Evaluation Metrics

As shown in Tab. 1, we introduce the common data benchmarks of different tasks for the evaluation. We follow the metrics used by each concept segmentation fields including weighted F-measure [53] (F_{β}^w), S-measure [20] (Sm), and mean absolute error (MAE) for salient object detection (SOD) and camouflaged object detection (COD), OBER [74] for shadow detection (SD) and transparent object segmentation (TOS), Intersection over Union (IoU) and Dice similarity coefficient for all lesion object segmentation (LOS) tasks, location mean absolute error (AL-MAE, CL-MAE, OH-MAE) and number accuracy (PN-ACC) for power battery detection (PBD) [95], and I-AUROC, I-AP, P-AUROC, P-AP, P-PRO for surface anomaly detection (AD). More details about these datasets and metrics can be found in the appendix.

3.2 Implementation Details

The architectures of SAM and SAM 2 are delineated in Fig. 2. Both share a similar framework, where the image encoder extracts multi-scale features from the input image. These features are then utilized by the mask decoder to generate prompt-specific masks, under the guidance of the information encoded by the prompt encoder. Compared with SAM, SAM 2 is enhanced with additional temporal modeling components, such as memory attention, memory encoder, and memory bank, to better leverage temporal information for video processing.

For simplicity and typicality, we uniformly evaluate the large versions of SAM and SAM 2 in all experiments on two NVIDIA V100 GPUs. The performance of related algorithms in various tasks are derived from the original papers, and we utilize the same evaluation tools. To thoroughly evaluate the capabilities of SAMs, we carefully conduct experiments with various prompt types, including basic modes like point (⊙) and bounding box (☐) with interaction, as well as automatic segmentation (☒) without interaction. SAM 2 also supports an additional mask type (⊛). Using these prompts, SAMs can focus on segmenting internal objects, allowing us to directly obtain the final predictions. In automatic mode (☒), we apply an *overlap filtering strategy (OFS)* based on the ground-truth mask (GT) to generate the final prediction. More details are available in the appendix.

3.3 Performance of Image Segmentation

• **Basic Mode.** Tabs. 2, 3, 4, 5, 6, 7, 8 separately list the performance comparisons among the different specialized models and SAMs (☒/☐/⊙) in the SOD, COD, SD, TOS, PBD, AD and LOS. Benefiting

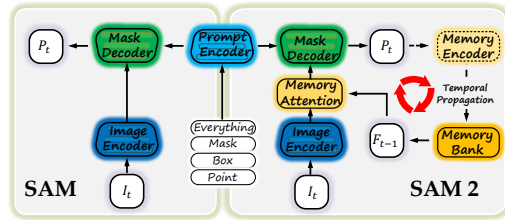


Figure 2: Architecture comparison for SAM and SAM 2. For the current frame I_t , SAM directly generates the corresponding prediction P_t . However, in SAM 2, the embedding F_{t-1} from the previous prediction P_{t-1} is fed into the encoding for I_t .

Table 2: Image SOD.

	DUTS [77]		PASCAL-S [41]		DUT-OMRON [88]		ECSSD [87]		HKU-IS [40]	
	F_{β}^{\uparrow}	Sm^{\uparrow}								
EDN [84]	0.844	0.892	0.827	0.865	0.770	0.850	0.918	0.927	0.908	0.924
MENet [81]	0.876	0.897	0.848	0.861	0.775	0.843	0.924	0.922	0.922	0.921
SAM (◻)	0.884	0.896	0.719	0.784	0.898	0.906	0.957	0.942	0.939	0.930
SAM (◻)	0.920	0.910	0.750	0.801	0.933	0.924	0.950	0.933	0.923	0.908
SAM (⊙)	0.886	0.888	0.760	0.803	0.931	0.929	0.964	0.949	0.927	0.919
SAM 2 (◻)	0.449	0.661	0.514	0.668	0.545	0.709	0.719	0.795	0.712	0.790
SAM 2 (◻)	0.929	0.921	0.752	0.801	0.941	0.932	0.958	0.941	0.928	0.914
SAM 2 (⊙)	0.807	0.815	0.634	0.688	0.772	0.777	0.777	0.766	0.759	0.756

Table 3: Image COD.

	COD10K [22]		CAMO [39]		NC4K [51]	
	F_{β}^{\uparrow}	Sm^{\uparrow}	F_{β}^{\uparrow}	Sm^{\uparrow}	F_{β}^{\uparrow}	Sm^{\uparrow}
SARNet [86]	0.820	0.885	0.844	0.874	0.851	0.889
ZoomNext [56]	0.838	0.898	0.859	0.888	0.865	0.900
SAM (◻)	0.694	0.786	0.631	0.707	0.698	0.773
SAM (◻)	0.863	0.882	0.853	0.854	0.878	0.885
SAM (⊙)	0.823	0.868	0.843	0.862	0.846	0.876
SAM 2 (◻)	0.260	0.587	0.170	0.493	0.237	0.550
SAM 2 (◻)	0.902	0.911	0.891	0.891	0.920	0.918
SAM 2 (⊙)	0.864	0.868	0.771	0.784	0.854	0.851

Table 4: Image SD. Table 5: Image TOS. Table 6: Image industrial PBD. —: Invalid value.

	ISTD [76]	SBU [75]
	BER \downarrow	BER \downarrow
SILT [89]	0.011	0.044
SARA [68]	0.018	0.029
SAM (◻)	0.205	0.256
SAM (◻)	0.150	0.141
SAM (⊙)	0.161	0.242
SAM 2 (◻)	0.336	0.425
SAM 2 (◻)	0.180	0.153
SAM 2 (⊙)	0.220	0.273

	Trans10K [85]
	BER \downarrow
EBLNet [29]	0.138
RFENet [27]	0.104
SAM (◻)	0.141
SAM (◻)	0.079
SAM (⊙)	0.057
SAM 2 (◻)	0.231
SAM 2 (◻)	0.069
SAM 2 (⊙)	0.255

	CFINet [90]	MDCNet[95]	SAM (◻)	SAM (◻)	SAM (⊙)	SAM 2 (◻)	SAM 2 (◻)	SAM 2 (⊙)	
	Regular	PN-ACC \uparrow AL-MAE \downarrow CL-MAE \downarrow OH-MAE \downarrow	0.688 4.022 3.807 3.950	0.954 2.337 1.841 2.042	— 0.147 1.653 0.877	— 160.145 516.093 —	— — — —	— — — —	0.128 1.318 1.696 1.311
Difficult	PN-ACC \uparrow AL-MAE \downarrow CL-MAE \downarrow OH-MAE \downarrow	0.543 4.960 4.988 3.977	0.760 2.440 2.098 2.109	— 0.133 1.740 1.010	— 43.217 301.011 —	— — — —	— — — —	0.196 1.601 1.620 1.330	101.321 294.389 — —
Tough	PN-ACC \uparrow AL-MAE \downarrow CL-MAE \downarrow OH-MAE \downarrow	0.328 4.945 4.662 3.699	0.512 2.000 1.465 1.629	— — 1.048 —	— 0.006 551.057 232.665	— — — —	— — — —	— 84.738 63.642 —	— — — —

Table 7: Image industrial AD.

	RD [19]	Patchcore [60]	SAM (◻)	SAM (◻)	SAM (⊙)	SAM 2 (◻)	SAM 2 (◻)	SAM 2 (⊙)	
	MVRec [3]	I-AUROC \uparrow I-AP \uparrow P-AUROC \uparrow P-AP \uparrow P-PRO \uparrow	98.6 99.2 97.8 99.4 58.0 93.9	55.1 77.8 51.1 27.5	53.3 79.8 93.2 62.8	52.3 72.7 32.5 75.7	72.7 91.6 84.5 28.8	94.9 97.7 97.8 78.4	89.6
Via4 [48]	I-AUROC \uparrow I-AP \uparrow P-AUROC \uparrow P-AP \uparrow P-PRO \uparrow	96.0 96.5 90.1 27.7 70.9	95.1 96.2 98.8 40.1 91.2	55.2 61.9 73.2 2.5 35.8	95.8 98.2 87.6 54.2 66.0	45.7 56.0 53.3 1.0 24.1	54.4 61.8 43.1 1.1 16.8	98.7 99.3 93.3 71.6 83.4	58.5 66.3 63.5 2.0 25.7
BTAD [55]	I-AUROC \uparrow I-AP \uparrow P-AUROC \uparrow P-AP \uparrow P-PRO \uparrow	93.7 98.5 95.8 51.7 72.3	94.7 98.9 97.8 52.0 75.2	75.5 66.5 47.8 3.5 17.7	86.1 93.9 72.6 29.0 41.8	64.9 82.5 79.9 15.2 49.7	52.5 59.6 29.3 2.0 4.2	81.0 90.4 76.5 30.7 51.0	71.8 82.2 79.1 47.9 58.3

Table 8: Image LOS. —: Unavailable value.

	COVID-19 [26]	BUSI [1]	ISIC-2018 [16]	Polyp-Five
	Dice \uparrow	IoU \uparrow	Dice \uparrow	IoU \uparrow
InfNet [26]	0.432	0.529	—	—
DECORNet [30]	0.403	0.695	—	—
AAUNet [10]	—	0.475	0.652	—
CMUNet [70]	—	0.545	0.830	—
MALUNet [61]	—	—	0.863	0.854
EGEUNet [62]	—	—	0.859	0.850
LDNet [92]	—	—	—	0.643
WeakPolyp [82]	—	—	—	0.749
SAM (◻)	0.431	0.705	0.477	0.670
SAM (◻)	0.858	0.885	0.849	0.859
SAM (⊙)	0.352	0.601	0.694	0.729
SAM 2 (◻)	0.244	0.612	0.156	0.528
SAM 2 (◻)	0.893	0.909	0.895	0.896
SAM 2 (⊙)	0.687	0.797	0.783	0.815
SAM 2 (◻)	0.600	0.761	0.708	0.553
SAM 2 (◻)	0.440	0.568	0.480	0.568
SAM 2 (⊙)	0.874	0.824	0.874	0.866
SAM 2 (⊙)	0.770	0.499	0.770	0.706

Table 9: Quantitative comparison of unified models with in-context learning mode.

	Image SOD		Image COD		TOS	Image SD	Image LOS				
	DUTS [77]	COD10K [22]	Trans10K [85]	SBU [75]	BER \downarrow	COVID-19 [26]	BUSI [1]	ISIC-2018 [16]	Polyp [24]		
	F_{β}^{\uparrow}	Sm^{\uparrow}	F_{β}^{\uparrow}	Sm^{\uparrow}		Dice \uparrow	IoU \uparrow	Dice \uparrow	IoU \uparrow	Dice \uparrow	IoU \uparrow
UniverSeg [6]	—	—	—	—	—	0.673	0.368	0.775	0.600	0.761	0.708
SegGPT [80]	0.387	0.628	0.404	0.653	0.306	0.131	0.553	0.336	0.603	0.480	0.568
Spider [96]	0.882	0.916	0.789	0.867	0.055	0.696	0.813	0.838	0.866	0.894	0.874
SAM 2 (⊙)	0.092	0.478	0.429	0.680	0.413	0.382	0.655	0.539	0.712	0.747	0.770

from the ability of box prompt to filter out large amounts of background information, SAMs (◻) generally perform well across most tasks. However, they still struggle with SD and PBD because these concepts lack clear, distinct objects and have minimal contrast with the background. Additionally, we observe SAM 2 (⊙) and SAM 2 (◻) are consistently weaker than their corresponding SAM variants.

• **In-Context Learning Mode.** Unlike SAM, SAM 2 incorporates a memory mechanism for temporal modeling. This enables SAM 2 to gain *in-context learning (ICL) capability using multiple concept samples rather than relying solely on prompts from the current image* [96, 80]. By providing additional exemplar samples and targeted guidance, it has the potential to better understand context-dependent (CD) concepts. To achieve this, we use 20 images from the training set, along with their corresponding masks, as contextual cues to help SAM 2 pre-encode and interpret different concepts. This setup is referred to as SAM 2 (⊙). As shown in Tab. 9, SAM 2 (⊙) demonstrates impressive performance in segmenting these varied CD concepts. Specifically, SAM 2 (⊙) shows competitive results on TOS and SD tasks and achieves a notable lead in COD and four LOS tasks, even surpassing SAM 2 (◻) in automatic mode. However, due to the lack of targeted training on CD concepts datasets, SAM 2 (⊙) still underperforms compared to UniverSeg [6] and Spider [96].

3.4 Performance of Video Segmentation

• **SAM for Video Data.** Given that SAM is not originally designed for video data, we evaluate it using two distinct setups: image-based and video-based prompting. In the image-based setup, the video is treated as a set of individual images, where individual GT-based prompts are used to generate

Table 10: Video LOS (Polyp Segmentation).

	CVC-612-T [32]		CVC-612-V [32]		CVC-300-TV [32]	
	Dice \uparrow	IoU \uparrow	Dice \uparrow	IoU \uparrow	Dice \uparrow	IoU \uparrow
PNSNet [32]	0.841	0.788	0.859	0.804	0.863	0.805
M ² SNet [93]	0.846	0.782	0.897	0.838	0.876	0.805
SAM (\square)	0.622	0.768	0.432	0.681	0.412	0.677
SAM (\square)	0.930	0.927	0.926	0.928	0.911	0.917
SAM (\odot)	0.798	0.818	0.693	0.750	0.504	0.634
SAM (Propagated \square)	0.079	0.460	0.138	0.528	0.136	0.533
SAM (Propagated \odot)	0.518	0.584	0.321	0.472	0.166	0.421
SAM 2 (1 \times \square)	0.798	0.866	0.762	0.846	0.897	0.906
SAM 2 (3 \times \square)	0.875	0.898	0.912	0.921	0.906	0.914
SAM 2 (5 \times \square)	0.909	0.925	0.920	0.928	0.914	0.920
SAM 2 (1 \times \odot)	0.900	0.919	0.754	0.843	0.905	0.913
SAM 2 (3 \times \odot)	0.905	0.925	0.918	0.926	0.929	0.933
SAM 2 (5 \times \odot)	0.919	0.933	0.926	0.933	0.936	0.939
SAM 2 (1 \times \star)	0.916	0.931	0.775	0.857	0.911	0.918
SAM 2 (3 \times \star)	0.915	0.933	0.930	0.937	0.944	0.947
SAM 2 (5 \times \star)	0.916	0.936	0.942	0.948	0.959	0.961

Table 11: Video SOD.

	DAVIS16 [57]		DAVSOD _E [25]		DAVSOD _N [25]		DAVSOD _H [25]	
	MAE \downarrow	Sm \uparrow	MAE \downarrow	Sm \uparrow	MAE \downarrow	Sm \uparrow	MAE \downarrow	Sm \uparrow
CoSTFormer [45]	0.014	0.921	0.061	0.806	0.090	0.711	—	—
MAMNet [94]	0.020	0.897	0.065	0.777	0.088	0.688	0.089	0.622
SAM (\square)	0.013	0.899	0.038	0.808	0.055	0.750	0.027	0.791
SAM (\square)	0.020	0.913	0.029	0.873	0.037	0.847	0.024	0.865
SAM (\odot)	0.009	0.927	0.030	0.879	0.044	0.828	0.030	0.828
SAM (Propagated \square)	0.042	0.712	0.091	0.614	0.108	0.587	0.098	0.544
SAM (Propagated \odot)	0.028	0.872	0.066	0.793	0.050	0.777	0.045	0.745
SAM 2 (1 \times \square)	0.006	0.936	0.051	0.773	0.055	0.769	0.062	0.652
SAM 2 (3 \times \square)	0.008	0.933	0.044	0.813	0.054	0.787	0.049	0.731
SAM 2 (5 \times \square)	0.007	0.936	0.044	0.812	0.047	0.805	0.050	0.687
SAM 2 (1 \times \odot)	0.005	0.949	0.043	0.800	0.062	0.736	0.060	0.645
SAM 2 (3 \times \odot)	0.005	0.950	0.033	0.853	0.052	0.788	0.047	0.727
SAM 2 (5 \times \odot)	0.005	0.954	0.027	0.872	0.041	0.820	0.039	0.754
SAM 2 (1 \times \star)	0.005	0.953	0.038	0.820	0.062	0.738	0.061	0.645
SAM 2 (3 \times \star)	0.005	0.957	0.027	0.874	0.049	0.793	0.047	0.729
SAM 2 (5 \times \star)	0.004	0.959	0.022	0.882	0.040	0.824	0.039	0.761

Table 12: Video COD.

	MoCA-Mask [14]		CAD [5]	
	MAE \downarrow	Sm \uparrow	MAE \downarrow	Sm \uparrow
SLT-Net [13]	0.027	0.637	0.031	0.696
ZoomNext [56]	0.010	0.734	0.020	0.757
SAM (\square)	0.010	0.638	0.019	0.735
SAM (\square)	0.005	0.817	0.017	0.851
SAM (\odot)	0.025	0.791	0.033	0.793
SAM (Propagated \square)	0.011	0.660	0.053	0.560
SAM (Propagated \odot)	0.074	0.604	0.103	0.551
SAM 2 (1 \times \square)	0.006	0.790	0.012	0.862
SAM 2 (3 \times \square)	0.005	0.798	0.009	0.874
SAM 2 (5 \times \square)	0.005	0.810	0.009	0.874
SAM 2 (1 \times \odot)	0.004	0.803	0.009	0.857
SAM 2 (3 \times \odot)	0.003	0.829	0.008	0.863
SAM 2 (5 \times \odot)	0.003	0.840	0.007	0.875
SAM 2 (1 \times \star)	0.004	0.820	0.008	0.883
SAM 2 (3 \times \star)	0.003	0.844	0.006	0.900
SAM 2 (5 \times \star)	0.002	0.860	0.005	0.913

Table 13: Video SD.

	VISAD-DS [48]		VISAD-MOS [48]	
	BER \downarrow	Sm \uparrow	BER \downarrow	Sm \uparrow
SANet [49]	0.131	0.259	0.131	0.259
SAM (\square)	0.146	0.342	0.146	0.342
SAM (\square)	0.091	0.125	0.091	0.125
SAM (\odot)	0.135	0.266	0.135	0.266
SAM (Propagated \square)	0.183	0.346	0.183	0.346
SAM (Propagated \odot)	0.287	0.342	0.287	0.342
SAM 2 (1 \times \square)	0.292	0.406	0.292	0.406
SAM 2 (3 \times \square)	0.283	0.367	0.283	0.367
SAM 2 (5 \times \square)	0.250	0.349	0.250	0.349
SAM 2 (1 \times \odot)	0.136	0.351	0.136	0.351
SAM 2 (3 \times \odot)	0.113	0.307	0.113	0.307
SAM 2 (5 \times \odot)	0.104	0.335	0.104	0.335
SAM 2 (1 \times \star)	0.106	0.317	0.106	0.317
SAM 2 (3 \times \star)	0.091	0.210	0.091	0.210
SAM 2 (5 \times \star)	0.070	0.172	0.070	0.172

Table 14: 3D LOS for the whole tumor (WT), tumor core (TC) and enhancing tumor (ET), and multiple sclerosis (MS).

(a) BraTS2020 [54]

	Flair			T1ce			T1			T2			Flair Dice \uparrow
	Dice \uparrow												
3D U-Net [15]	0.900	0.807	0.792	0.900	0.807	0.792	0.900	0.807	0.792	0.900	0.807	0.792	0.803
EoFormer [65]	0.908	0.864	0.832	0.908	0.864	0.832	0.908	0.864	0.832	0.908	0.864	0.832	0.803
SAM 2 (1 \times \square)	0.566	0.574	0.579	0.566	0.574	0.582	0.566	0.570	0.579	0.566	0.574	0.579	0.635
SAM 2 (3 \times \square)	0.560	0.574	0.579	0.566	0.574	0.582	0.566	0.570	0.618	0.560	0.574	0.579	0.638
SAM 2 (5 \times \square)	0.555	0.574	0.670	0.567	0.615	0.582	0.566	0.578	0.579	0.555	0.574	0.670	0.636
SAM 2 (1 \times \odot)	0.700	0.683	0.643	0.681	0.684	0.592	0.675	0.615	0.558	0.700	0.683	0.550	0.630
SAM 2 (3 \times \odot)	0.788	0.753	0.700	0.747	0.780	0.707	0.761	0.728	0.659	0.788	0.753	0.650	0.630
SAM 2 (5 \times \odot)	0.835	0.793	0.723	0.804	0.794	0.733	0.799	0.748	0.676	0.835	0.793	0.670	0.630
SAM 2 (1 \times \star)	0.706	0.698	0.645	0.700	0.676	0.639	0.670	0.639	0.587	0.706	0.698	0.647	0.728
SAM 2 (3 \times \star)	0.864	0.803	0.760	0.841	0.808	0.775	0.810	0.765	0.734	0.864	0.803	0.760	0.763
SAM 2 (5 \times \star)	0.889	0.843	0.796	0.871	0.838	0.803	0.860	0.815	0.783	0.889	0.843	0.796	0.768

(b) ISBI2015 [8]

	Flair			T1			T2			Flair Dice \uparrow
	Dice \uparrow									
DRU-Net [64]	0.900	0.807	0.792	0.900	0.807	0.792	0.900	0.807	0.792	0.803
ArtU-Net [28]	0.908	0.864	0.832	0.908	0.864	0.832	0.908	0.864	0.832	0.803
SAM 2 (1 \times \square)	0.566	0.574	0.579	0.566	0.574	0.582	0.566	0.570	0.579	0.635
SAM 2 (3 \times \square)	0.560	0.574	0.579	0.566	0.574	0.582	0.566	0.570	0.618	0.638
SAM 2 (5 \times \square)	0.555	0.574	0.670	0.567	0.615	0.582	0.566	0.578	0.579	0.636
SAM 2 (1 \times \odot)	0.700	0.683	0.643	0.681	0.684	0.592	0.675	0.615	0.558	0.630
SAM 2 (3 \times \odot)	0.788	0.753	0.700	0.747	0.780	0.707	0.761	0.728	0.659	0.630
SAM 2 (5 \times \odot)	0.835	0.793	0.723	0.804	0.794	0.733	0.799	0.748	0.676	0.630
SAM 2 (1 \times \star)	0.706	0.698	0.645	0.700	0.676	0.639	0.670	0.639	0.587	0.728
SAM 2 (3 \times \star)	0.864	0.803	0.760	0.841	0.808	0.775	0.810	0.765	0.734	0.763
SAM 2 (5 \times \star)	0.889	0.843	0.796	0.871	0.838	0.803	0.860	0.815	0.783	0.768

Table 15: Robustness analysis under various random perturbations: a random perturbation (0–10%) in the length of the shorter side of \square , a random displacement of up to 10 pixels in the coordinates of \odot , and random erosion or dilation with 5 iterations in \star . Δ denotes the relative performance change compared to the results with ideal prompts without perturbations.

(a) Image Data

	DUTS [77]		MVTEC-AD [3]				
	F \uparrow	Sm \uparrow	I-AUROC \uparrow	I-AP \uparrow	P-AUROC \uparrow	P-AP \uparrow	P-PRO \uparrow
SAM (\square)	0.894 \pm 1.1E-03	0.888 \pm 1.1E-03	0.726 \pm 7.0E-04	0.917 \pm 2.00E-04	0.845 \pm 1.0E-04	0.289 \pm 2.0E-04	0.630 \pm 2.0E-04
Δ	\downarrow 2.75%	\downarrow 2.35%	\downarrow 6.66%	\downarrow 1.22%	\downarrow 10.11%	\downarrow 21.73%	\downarrow 10.29%
SAM (\odot)	0.831 \pm 2.3E-03	0.852 \pm 2.3E-03	0.585 \pm 6.3E-03	0.821 \pm 2.4E-03	0.924 \pm 1.9E-03	0.430 \pm 8.7E-03	0.731 \pm 1.8E-03
Δ	\downarrow 6.30%	\downarrow 4.01%	\uparrow 9.76%	\downarrow 2.87%	\downarrow 0.88%	\downarrow 3.46%	\downarrow 3.50%
SAM 2 (\square)	0.857 \pm 2.3E-03	0.864 \pm 1.3E-03	0.779 \pm 5.0E-04	0.929 \pm 2.00E-04	0.847 \pm 1.0E-04	0.369 \pm 1.0E-04	0.629 \pm 1.0E-04
Δ	\downarrow 7.75%	\downarrow 6.09%	\uparrow 7.11%	\uparrow 1.38%	\uparrow 10.22%	\downarrow 28.09%	\downarrow 10.08%
SAM 2 (\odot)	0.773 \pm 1.4E-03	0.792 \pm 9.0E-04	0.939 \pm 6.7E-03	0.970 \pm 3.4E-03	0.975 \pm 1.0E-03	0.774 \pm 3.9E-03	0.878 \pm 2.2E-03
Δ	\downarrow 4.20%	\downarrow 2.77%	\downarrow 1.05%	\downarrow 0.70%	\downarrow 0.27%	\downarrow 1.34%	\downarrow 1.96%

(b) Video Data</

- **SAM 2 for Video Data.** Since objects often exhibit limited motion at the start of a video sequence, we introduce prompt information from intermediate frames. Specifically, we collect results under three setups: by introducing 1 frame, 3 frames, and 5 frames, referred to as “1×”, “3×”, and “5×”. In “1×”, only the first frame is used as the object prompt. In “3×” and “5×”, additional frames are introduced at the $\{\frac{i}{3}\}_{i=1}^2$ and the $\{\frac{i}{5}\}_{i=1}^4$ points of the sequence, respectively.

All experimental results are listed in Tabs. 10, 11, 12, 13. We can see that SAM performs best with box prompts, followed by point prompts, and shows the lowest performance in automatic mode. This performance gap is particularly evident in challenging tasks such as COD, SD, LOS, and in complex datasets like DAVSOD_N and DAVSOD_H in SOD. However, with a propagation-based prompt strategy, the point form surpasses the box form and even outperforms existing domain-specific specialized models in video SOD. For SAM 2, mask prompts yield the highest performance, followed by point and then box prompts. Both point and mask prompts show stable improvements as the number of prompts increases. In contrast, box prompts exhibit inconsistent gains, particularly on complex datasets like DAVSOD_E and DAVSOD_H. Due to its built-in temporal modeling, SAM 2 demonstrates strong adaptability in video tasks, often surpassing domain-specific models with just a single prompt. Notably, with a propagation strategy using point prompts, SAM can outperform SAM 2 with single-point prompts on DAVSOD_N and DAVSOD_H datasets.

3.5 Performance of 3D Segmentation

Since some 3D medical lesion image sequences consist of pure background images without foreground, we only evaluate the performance of SAM 2 based on our proposed bidirectional inference strategy. Specifically, we first traverse the entire 3D sequence and select the sequence with the largest foreground region mask as the anchor. Then, the entire sequence is split into two parts, and SAM 2 treats each part as a separate video sequence for bidirectional inference, using the shared starting frame. The combined results are used as predictions for the entire slice sequence. Each video sequence is inferred using the “1×”, “3×”, and “5×” approaches, similar to the video setting. As shown in Tab. 14, SAM 2 (5×) achieves excellent performance, even surpassing specialized models like 3D U-Net and DRU-Net. This demonstrates the effectiveness of the bidirectional inference strategy and multi-frame mask prompts for SAM 2.

3.6 Prompts Robustness Analysis

Existing evaluation schemes usually use target GT to construct ideal prompts. However, this does not accurately reflect real-world scenarios, as randomness in practical use can impact the model’s performance. To simulate the prompt randomness, we design a new evaluation scheme that introduces random perturbations to GT-based prompts. These perturbed prompts guide inference, enabling an assessment of the model’s robustness. In Tab. 15, we present a robustness evaluation of SAM and SAM 2 on various image and video tasks. Across different datasets, perturbed prompts lead to noticeable performance fluctuations in both models. Consistent performance drops are observed for SAM and SAM 2 in the DUTS and DAVIS16 datasets. However, in other datasets, perturbed prompts occasionally help the models surpass ideal prompts. Additionally, the low standard deviation across multiple random perturbations (typically on the order of 1e-3) indicates both models’ high sensitivity to perturbations. This shows a notable difference from results with ideal prompts, but with limited variation across multiple perturbations. Therefore, prompt accuracy in practical applications significantly impacts SAM segmentation performance, which is overlooked by most current studies.

3.7 Performance Summary

Through the aforementioned comprehensive evaluation, the performance of SAMs on context-dependent concepts segmentation can be summarized as follows: **I)** Generally speaking, the box prompt is the most advantageous type of prompt for SAMs. **II)** SAM 2 is not always superior to SAM and performs worse on tasks involving everything and point prompts. **III)** SAM 2 has the potential for in-context learning (ICL) predictions, but further exploration is needed. **IV)** In video segmentation tasks, SAM successfully completes the one-shot video object segmentation task by propagating the point prompt from the first frame, owing to the large tolerance provided by point propagation. This shows that SAM, originally developed for images, can handle video tasks effectively. SAM 2 performs even better and surpasses specialized models. **V)** In 3D medical lesion

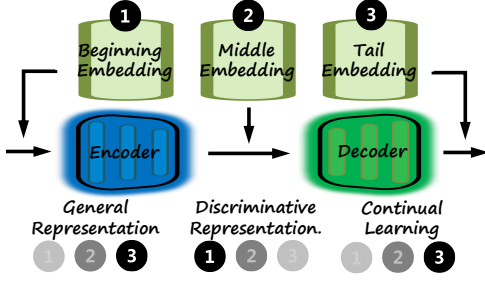


Figure 3: Architecture with three different embedding positions.

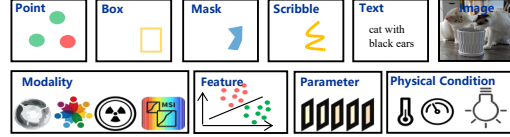


Figure 4: Diverse prompt types.

segmentation, the proposed bidirectional inference strategy and multi-frame mask prompts help SAM 2 achieve excellent performance, even surpassing specialized models. **VI)** SAMs perform poorly on non-material or extremely small target concepts, such as shadows or power battery plate endpoints. **VII)** SAMs are highly sensitive to the accuracy of prompts.

4 Outlook for SAM 3

In this section, we analyze the characteristics of current popular unified segmentation models, including SAM [37], SAM 2 [59], UniverSeg [6], SegGPT [80], and Spider [96], across the following aspects: architecture, prompt types, prompt-target interaction, training data and strategies. In this way, we can provide a meaningful outlook for SAM 3.

- **Architecture.** Unified segmentation models typically utilize a straightforward encoder-decoder framework without elaborate modules. They segment prompt-defined concepts through interactions between prompt and target features. As shown in Fig. 3, these models employ different strategies for embedding prompts: UniverSeg and SegGPT use beginning embedding, SAM and SAM 2 use middle embedding, and Spider uses tail embedding. Key capabilities for a strong segmentation model include representing general concepts, distinguishing different features, and enabling continuous learning. The position of prompt embedding significantly impacts these capabilities. For instance, beginning embedding tightly integrates the prompt with the concept from the outset, enhancing discriminative representation by focusing on concept distinctions. However, it reduces general representation capability and complicates continual learning, requiring fine-tuning of the entire network for new concepts. Conversely, tail embedding offers a different strategy, while middle embedding provides a more balanced solution. Future advancements in prompt information propagation could address tail embedding’s weaknesses in discriminative representation, making it more competitive.

- **Prompt Types.** Fig. 4 illustrates various prompt types used or yet to be utilized in unified models. Currently, popular types include point, box, mask, text, and image prompts. To improve segmentation across diverse scenarios, exploring new prompt types is key. Potential directions include: **I)** Modalities like depth maps, infrared images, multispectral images, and X-rays can provide valuable context beyond traditional RGB. These data types help models better understand scene and object structures, especially in medical imaging and industrial inspection. **II)** Predefined features or attributes, such as high-dimensional vectors or task-specific attributes, can guide segmentation, particularly in domain-specific tasks. For example, in industrial battery detection, feature prompts representing pristine electrodes can help identify anomalies more accurately. **III)** These prompts dynamically adjust the model’s parameters, similar to learnable prompts but focused on optimizing weights and structure. Existing image restoration methods have shown that learnable parameter cues can capture unknown degradation types, improving tasks like denoising, deblurring, and restoration across various domains. **IV)** In sensor-based scenarios, prompts can use real-time environmental data, such as temperature or motion, to guide system behavior. For instance, wearable medical devices can personalize responses based on individual physiological data, while industrial systems can adapt based on specific environmental conditions for optimized user experience.

Moreover, the current isolated prompt strategy often lacks sufficient context. In real-world applications, multiple prompt types can be gathered simultaneously. Developing a unified prompt embedding

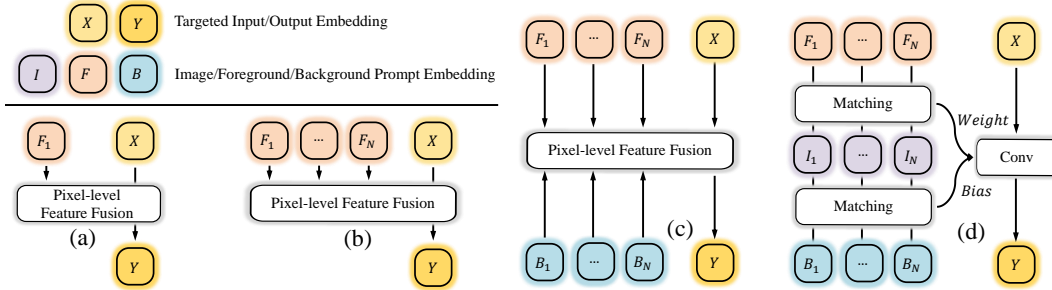


Figure 5: Four types of feature interaction between visual prompts and current target input.

mechanism to integrate these types could create a truly unified structure, enhancing segmentation capabilities across diverse scenarios.

- Prompt-Target Interaction.** The effective interaction between target features and prompt features is the key to drive a unified model to distinguish different concepts based on limited prompts. SegGPT uses a single foreground prompt embedding for pixel-level feature fusion (Fig. 5(a)). UniverSeg employs group foreground prompt embedding for the same purpose (Fig. 5(b)), while SAM 2 (⊙) uses both foreground and background group prompt embeddings (Fig. 5(c)). Spider condenses high-level image-foreground and image-background matching knowledge to generate a concept filter that facilitates feature interaction (Fig. 5(d)). Group prompt embeddings are gaining popularity as they explicitly enhance prompt information. Pixel-level fusion excels in perceiving consistent target appearances, making it effective for context-independent (CI) concepts. However, appearance variations may cause ambiguity, limiting its effectiveness for context-dependent (CD) concepts. In contrast, high-level concept filtering relies on abstract information, allowing Spider to excel in CD concepts. While Spider can handle CI tasks, it tends to focus more on object localization, overlooking appearance details. Future work could combine both interaction forms to improve segmentation for both CI and CD concepts.

- Training Data and Strategies.** Most unified models aim to obtain strong representations from large datasets to improve generalization across various concepts. However, there is no benchmark dataset specifically for unified segmentation models. Spider is trained exclusively on datasets with context-dependent (CD) concepts, while others use context-independent (CI) datasets. Integrating both CD and CI concepts with a self-training strategy, similar to SAM, could create a large-scale CI-CD joint benchmark by annotating different concepts for each image, benefiting segmentation and enhancing model discriminative power. Additionally, concept-balanced training is essential. SegGPT assigns different sampling weights to balance concepts from the data scale perspective, while SAM simulates interactive segmentation by iteratively refining masks with initial prompts. In contrast, UniverSeg focuses on enhancing data sample diversity. Spider considers concept balance in propagation, but its resource limitations prevent simultaneous training on multiple concepts. A potential future direction could be adjusting learning rates and update directions based on concept performance, inspired by optimizers like SGD and Adam [36], to improve convergence and balance across concepts.

5 Conclusion

This paper provides a comprehensive evaluation of SAMs (SAM and SAM 2) in segmenting context-dependent (CD) concepts across 11 categories with 2D, 3D, and video data in natural, medical, and industrial scenes. First, we establish a unified inference framework for SAM and SAM 2 to assess prompt types, strategies, and robustness. Next, we conduct extensive experiments on SAMs across different concepts in image, video, and 3D data, during which we also demonstrate the effectiveness of the proposed propagation-based prompt strategy, bidirectional inference strategy, and in context learning-based inference mode. This enables us to discuss the strengths and limitations of SAMs in segmenting CD concepts. Finally, we summarize the characteristics of various unified segmentation models and provide suggestions for improvement. Based on these results and insights, we believe this work will establish a baseline for CD concept segmentation and encourage further enhancement of SAM 2 in anticipation of SAM 3.

References

- [1] W. Al-Dhabyani, M. Gomaa, H. Khaled, and A. Fahmy. Dataset of breast ultrasound images. *Data in Brief*, 28:104863, 2020.
- [2] L. W. Barsalou. Context-independent and context-dependent information in concepts. *Memory & Cognition*, 10(1):82–93, 1982.
- [3] P. Bergmann, M. Fauser, D. Sattlegger, and C. Steger. Mvtec ad—a comprehensive real-world dataset for unsupervised anomaly detection. In *Proceedings of IEEE Conference on Computer Vision and Pattern Recognition*, pages 9592–9600, 2019.
- [4] J. Bernal, F. J. Sánchez, G. Fernández-Esparrach, D. Gil, C. Rodríguez, and F. Vilariño. Window maps for accurate polyp highlighting in colonoscopy: Validation vs. saliency maps from physicians. *Computerized Medical Imaging and Graphics*, 43:99–111, 2015.
- [5] P. Bideau and E. Learned-Miller. It’s moving! a probabilistic model for causal motion segmentation in moving camera videos. In *Proceedings of European Conference on Computer Vision*, pages 433–449, 2016.
- [6] V. I. Butoi, J. J. G. Ortiz, T. Ma, M. R. Sabuncu, J. Guttag, and A. V. Dalca. Universeg: Universal medical image segmentation. In *Proceedings of IEEE International Conference on Computer Vision*, pages 21438–21451, 2023.
- [7] H. Caesar, J. Uijlings, and V. Ferrari. Coco-stuff: Thing and stuff classes in context. In *Proceedings of IEEE Conference on Computer Vision and Pattern Recognition*, pages 1209–1218, 2018.
- [8] A. Carass, S. Roy, A. Jog, J. L. Cuzzocreo, E. Magrath, A. Gherman, J. Button, J. Nguyen, F. Prados, C. H. Sudre, et al. Longitudinal multiple sclerosis lesion segmentation: resource and challenge. *NeuroImage*, 148:77–102, 2017.
- [9] G. Chen, K. Han, and K.-Y. K. Wong. Tom-net: Learning transparent object matting from a single image. In *Proceedings of IEEE Conference on Computer Vision and Pattern Recognition*, pages 9233–9241, 2018.
- [10] G. Chen, L. Li, Y. Dai, J. Zhang, and M. H. Yap. Aau-net: An adaptive attention u-net for breast lesions segmentation in ultrasound images. *IEEE Transactions on Medical Imaging*, 42(5):1289–1300, 2023.
- [11] T. Chen, L. Zhu, C. Ding, R. Cao, Y. Wang, Z. Li, L. Sun, P. Mao, and Y. Zang. Sam fails to segment anything?—sam-adapter: Adapting sam in underperformed scenes: Camouflage, shadow, medical image segmentation, and more. *arXiv preprint arXiv:2304.09148*, 2023.
- [12] Z. Chen, Q. Xu, R. Cong, and Q. Huang. Global context-aware progressive aggregation network for salient object detection. In *Proceedings of AAAI Conference on Artificial Intelligence*, pages 10599–10606, 2020.
- [13] X. Cheng, H. Xiong, D. Fan, Y. Zhong, M. Harandi, T. Drummond, and Z. Ge. Implicit motion handling for video camouflaged object detection. In *Proceedings of IEEE Conference on Computer Vision and Pattern Recognition*, pages 13854–13863, 2022.
- [14] X. Cheng, H. Xiong, D.-P. Fan, Y. Zhong, M. Harandi, T. Drummond, and Z. Ge. Implicit motion handling for video camouflaged object detection. In *Proceedings of IEEE Conference on Computer Vision and Pattern Recognition*, pages 13864–13873, 2022.
- [15] Ö. Çiçek, A. Abdulkadir, S. S. Lienkamp, T. Brox, and O. Ronneberger. 3d u-net: Learning dense volumetric segmentation from sparse annotation. In S. Ourselin, L. Joskowicz, M. R. Sabuncu, G. B. Ünal, and W. M. W. III, editors, *Proceedings of International Conference on Medical Image Computing and Computer-Assisted Intervention*, volume 9901 of *Lecture Notes in Computer Science*, pages 424–432, 2016.

- [16] N. Codella, V. Rotemberg, P. Tschandl, M. E. Celebi, S. Dusza, D. Gutman, B. Helba, A. Kalloo, K. Liopyris, M. Marchetti, et al. Skin lesion analysis toward melanoma detection 2018: A challenge hosted by the international skin imaging collaboration (isic). *arXiv preprint arXiv:1902.03368*, 2019.
- [17] R. Cong, H. Yang, Q. Jiang, W. Gao, H. Li, C. Wang, Y. Zhao, and S. Kwong. Bcs-net: Boundary, context, and semantic for automatic covid-19 lung infection segmentation from ct images. *IEEE Transactions on Instrumentation and Measurement*, 71:1–11, 2022.
- [18] M. Cordts, M. Omran, S. Ramos, T. Rehfeld, M. Enzweiler, R. Benenson, U. Franke, S. Roth, and B. Schiele. The cityscapes dataset for semantic urban scene understanding. In *Proceedings of IEEE Conference on Computer Vision and Pattern Recognition*, pages 3213–3223, 2016.
- [19] H. Deng and X. Li. Anomaly detection via reverse distillation from one-class embedding. In *Proceedings of IEEE Conference on Computer Vision and Pattern Recognition*, pages 9727–9736, 2022.
- [20] D.-P. Fan, M.-M. Cheng, Y. Liu, T. Li, and A. Borji. Structure-measure: A new way to evaluate foreground maps. In *Proceedings of IEEE International Conference on Computer Vision*, pages 4548–4557, 2017.
- [21] D.-P. Fan, G.-P. Ji, M.-M. Cheng, and L. Shao. Concealed object detection. *IEEE Transactions on Pattern Analysis and Machine Intelligence*, 44(10):6024–6042, 2021.
- [22] D.-P. Fan, G.-P. Ji, G. Sun, M.-M. Cheng, J. Shen, and L. Shao. Camouflaged object detection. In *Proceedings of IEEE Conference on Computer Vision and Pattern Recognition*, pages 2777–2787, 2020.
- [23] D.-P. Fan, G.-P. Ji, P. Xu, M.-M. Cheng, C. Sakaridis, and L. Van Gool. Advances in deep concealed scene understanding. *Visual Intelligence*, 1(1):16, 2023.
- [24] D.-P. Fan, G.-P. Ji, T. Zhou, G. Chen, H. Fu, J. Shen, and L. Shao. Pranet: Parallel reverse attention network for polyp segmentation. In *Proceedings of International Conference on Medical Image Computing and Computer-Assisted Intervention*, pages 263–273, 2020.
- [25] D.-P. Fan, W. Wang, M.-M. Cheng, and J. Shen. Shifting more attention to video salient object detection. In *Proceedings of IEEE Conference on Computer Vision and Pattern Recognition*, pages 8554–8564, 2019.
- [26] D.-P. Fan, T. Zhou, G.-P. Ji, Y. Zhou, G. Chen, H. Fu, J. Shen, and L. Shao. Inf-net: Automatic covid-19 lung infection segmentation from ct images. *IEEE Transactions on Medical Imaging*, 39(8):2626–2637, 2020.
- [27] K. Fan, C. Wang, Y. Wang, C. Wang, R. Yi, and L. Ma. Rfenet: Towards reciprocal feature evolution for glass segmentation. In *Proceedings of International Joint Conference on Artificial Intelligence*, pages 717–725, 2023.
- [28] M. Hashemi, M. Akhbari, and C. Jutten. Delve into multiple sclerosis (MS) lesion exploration: A modified attention u-net for MS lesion segmentation in brain MRI. *Computers in Biology and Medicine*, 145:105402, 2022.
- [29] H. He, X. Li, G. Cheng, J. Shi, Y. Tong, G. Meng, V. Prinet, and L. Weng. Enhanced boundary learning for glass-like object segmentation. In *Proceedings of IEEE International Conference on Computer Vision*, pages 15839–15848, 2021.
- [30] J. Hu, Y. Yang, X. Guo, B. Peng, H. Huang, and T. Ma. Decor-net: A covid-19 lung infection segmentation network improved by emphasizing low-level features and decorrelating features. In *IEEE International Symposium on Biomedical Imaging*, pages 1–5, 2023.
- [31] D. Jha, P. H. Smedsrud, M. A. Riegler, P. Halvorsen, T. d. Lange, D. Johansen, and H. D. Johansen. Kvasir-seg: A segmented polyp dataset. In *Proceedings of International Conference on Multimedia Modeling*, pages 451–462, 2020.

- [32] G.-P. Ji, Y.-C. Chou, D.-P. Fan, G. Chen, H. Fu, D. Jha, and L. Shao. Progressively normalized self-attention network for video polyp segmentation. In *Proceedings of International Conference on Medical Image Computing and Computer-Assisted Intervention*, pages 142–152, 2021.
- [33] G.-P. Ji, D.-P. Fan, P. Xu, M.-M. Cheng, B. Zhou, and L. Van Gool. Sam struggles in concealed scenes—empirical study on "segment anything". *arXiv preprint arXiv:2304.06022*, 2023.
- [34] W. Ji, J. Li, Q. Bi, T. Liu, W. Li, and L. Cheng. Segment anything is not always perfect: An investigation of sam on different real-world applications. *Machine Intelligence Research*, 21:617–630, 2024.
- [35] L. Ke, M. Ye, M. Danelljan, Y. Liu, Y.-W. Tai, C.-K. Tang, and F. Yu. Segment anything in high quality. In *Proceedings of International Conference and Workshop on Neural Information Processing Systems*, 2024.
- [36] D. P. Kingma. Adam: A method for stochastic optimization. In *Proceedings of International Conference on Learning Representations*, 2015.
- [37] A. Kirillov, E. Mintun, N. Ravi, H. Mao, C. Rolland, L. Gustafson, T. Xiao, S. Whitehead, A. C. Berg, W.-Y. Lo, et al. Segment anything. In *Proceedings of IEEE International Conference on Computer Vision*, pages 4015–4026, 2023.
- [38] H. Lamdouar, C. Yang, W. Xie, and A. Zisserman. Betrayed by motion: Camouflaged object discovery via motion segmentation. 2020.
- [39] T.-N. Le, T. V. Nguyen, Z. Nie, M.-T. Tran, and A. Sugimoto. Anabranh network for camouflaged object segmentation. *Computer Vision and Image Understanding*, 184:45–56, 2019.
- [40] G. Li and Y. Yu. Visual saliency based on multiscale deep features. In *Proceedings of IEEE Conference on Computer Vision and Pattern Recognition*, pages 5455–5463, 2015.
- [41] Y. Li, X. Hou, C. Koch, J. M. Rehg, and A. L. Yuille. The secrets of salient object segmentation. In *Proceedings of IEEE Conference on Computer Vision and Pattern Recognition*, pages 280–287, 2014.
- [42] S. Lian and H. Li. Evaluation of segment anything model 2: The role of sam2 in the underwater environment. *arXiv preprint arXiv:2408.02924*, 2024.
- [43] S. Lian, Z. Zhang, H. Li, W. Li, L. T. Yang, S. Kwong, and R. Cong. Diving into underwater: Segment anything model guided underwater salient instance segmentation and a large-scale dataset. In *Proceedings of International Conference on Machine Learning*, 2024.
- [44] J. Lin, Z. He, and R. W. Lau. Rich context aggregation with reflection prior for glass surface detection. In *Proceedings of IEEE Conference on Computer Vision and Pattern Recognition*, pages 13415–13424, 2021.
- [45] N. Liu, K. Nan, W. Zhao, X. Yao, and J. Han. Learning complementary spatial-temporal transformer for video salient object detection. *IEEE Transactions on Neural Networks and Learning Systems*, 35(8):10663–10673, 2024.
- [46] W. Liu, X. Shen, C.-M. Pun, and X. Cun. Explicit visual prompting for low-level structure segmentations. In *Proceedings of IEEE Conference on Computer Vision and Pattern Recognition*, pages 19434–19445, 2023.
- [47] Y. Liu, M. Zhu, H. Li, H. Chen, X. Wang, and C. Shen. Matcher: Segment anything with one shot using all-purpose feature matching. *arXiv preprint arXiv:2305.13310*, 2023.
- [48] X. Lu, Y. Cao, S. Liu, C. Long, Z. Chen, X. Zhou, Y. Yang, and C. Xiao. Video shadow detection via spatio-temporal interpolation consistency training. In *Proceedings of IEEE Conference on Computer Vision and Pattern Recognition*, pages 3116–3125, 2022.

- [49] X. Lu, Y. Cao, S. Liu, C. Long, Z. Chen, X. Zhou, Y. Yang, and C. Xiao. Video shadow detection via spatio-temporal interpolation consistency training. In *Proceedings of IEEE Conference on Computer Vision and Pattern Recognition*, pages 3106–3115, 2022.
- [50] Z. Luo, N. Liu, W. Zhao, X. Yang, D. Zhang, D.-P. Fan, F. Khan, and J. Han. Vscope: General visual salient and camouflaged object detection with 2d prompt learning. In *Proceedings of IEEE Conference on Computer Vision and Pattern Recognition*, pages 17169–17180, 2024.
- [51] Y. Lv, J. Zhang, Y. Dai, A. Li, B. Liu, N. Barnes, and D.-P. Fan. Simultaneously localize, segment and rank the camouflaged objects. In *Proceedings of IEEE Conference on Computer Vision and Pattern Recognition*, pages 11591–11601, 2021.
- [52] J. Ma, Y. He, F. Li, L. Han, C. You, and B. Wang. Segment anything in medical images. *Nature Communications*, 15(1):654, 2024.
- [53] R. Margolin, L. Zelnik-Manor, and A. Tal. How to evaluate foreground maps? In *Proceedings of IEEE Conference on Computer Vision and Pattern Recognition*, pages 248–255, 2014.
- [54] R. Mehta, A. Filos, U. Baid, C. Sako, R. McKinley, M. Rebsamen, K. Datwyler, R. Meier, P. Radojewski, G. K. Murugesan, et al. Qu-brats: Miccai brats 2020 challenge on quantifying uncertainty in brain tumor segmentation-analysis of ranking scores and benchmarking results. *arXiv preprint arXiv:2112.10074*, 2021.
- [55] P. Mishra, R. Verk, D. Fornasier, C. Piciarelli, and G. L. Foresti. Vt-adl: A vision transformer network for image anomaly detection and localization. In *Proceedings of International Symposium on Industrial Electronics*, pages 01–06, 2021.
- [56] Y. Pang, X. Zhao, T.-Z. Xiang, L. Zhang, and H. Lu. Zoomnext: A unified collaborative pyramid network for camouflaged object detection. *IEEE Transactions on Pattern Analysis and Machine Intelligence*, 2024.
- [57] F. Perazzi, J. Pont-Tuset, B. McWilliams, L. Van Gool, M. Gross, and A. Sorkine-Hornung. A benchmark dataset and evaluation methodology for video object segmentation. In *Proceedings of IEEE Conference on Computer Vision and Pattern Recognition*, pages 724–732, 2016.
- [58] X. Qin, H. Dai, X. Hu, D.-P. Fan, L. Shao, and L. Van Gool. Highly accurate dichotomous image segmentation. In *ECCV*, pages 38–56, 2022.
- [59] N. Ravi, V. Gabeur, Y.-T. Hu, R. Hu, C. Ryali, T. Ma, H. Khedr, R. Rädle, C. Rolland, L. Gustafson, et al. Sam 2: Segment anything in images and videos. *arXiv preprint arXiv:2408.00714*, 2024.
- [60] K. Roth, L. Pemula, J. Zepeda, B. Schölkopf, T. Brox, and P. V. Gehler. Towards total recall in industrial anomaly detection. In *Proceedings of IEEE Conference on Computer Vision and Pattern Recognition*, pages 14298–14308, 2022.
- [61] J. Ruan, S. Xiang, M. Xie, T. Liu, and Y. Fu. Malunet: A multi-attention and light-weight unet for skin lesion segmentation. In *IEEE International Conference on Bioinformatics and Biomedicine*, pages 1150–1156, 2022.
- [62] J. Ruan, M. Xie, J. Gao, T. Liu, and Y. Fu. Ege-unet: An efficient group enhanced unet for skin lesion segmentation. In *Proceedings of International Conference on Medical Image Computing and Computer-Assisted Intervention*, pages 481–490, 2023.
- [63] A. N. Rumaksari, S. Sumpeno, and A. D. Wibawa. Background subtraction using spatial mixture of gaussian model with dynamic shadow filtering. In *Proceedings of International Seminar on Intelligent Technology and Its Applications*, pages 296–301, 2017.
- [64] B. Sarica, D. Z. Seker, and B. Bayram. A dense residual u-net for multiple sclerosis lesions segmentation from multi-sequence 3d MR images. *International Journal of Medical Informatics*, 170:104965, 2023.
- [65] D. She, Y. Zhang, Z. Zhang, H. Li, Z. Yan, and X. Sun. Eoformer: Edge-oriented transformer for brain tumor segmentation. In *Proceedings of International Conference on Medical Image Computing and Computer-Assisted Intervention*, pages 333–343, 2023.

- [66] J. Silva, A. Histace, O. Romain, X. Dray, and B. Granado. Toward embedded detection of polyps in wce images for early diagnosis of colorectal cancer. *International Journal of Computer Assisted Radiology and Surgery*, 9:283–293, 2014.
- [67] P. Skurowski, H. Abdulameer, J. Błaszczuk, T. Depta, A. Kornacki, and P. Koziel. Animal camouflage analysis: Chameleon database. *Unpublished Manuscript*, 2018.
- [68] J. Sun, K. Xu, Y. Pang, L. Zhang, H. Lu, G. P. Hancke, and R. W. H. Lau. Adaptive illumination mapping for shadow detection in raw images. In *Proceedings of IEEE International Conference on Computer Vision*, pages 12663–12672, 2023.
- [69] N. Tajbakhsh, S. R. Gurudu, and J. Liang. Automated polyp detection in colonoscopy videos using shape and context information. *IEEE Transactions on Medical Imaging*, 35(2):630–644, 2015.
- [70] F. Tang, L. Wang, C. Ning, M. Xian, and J. Ding. Cmu-net: A strong convmixer-based medical ultrasound image segmentation network. In *IEEE International Symposium on Biomedical Imaging*, pages 1–5, 2023.
- [71] L. Tang and B. Li. Evaluating sam2’s role in camouflaged object detection: From sam to sam2. *arXiv preprint arXiv:2407.21596*, 2024.
- [72] Z. Tu, T. Xia, C. Li, X. Wang, Y. Ma, and J. Tang. Rgb-t image saliency detection via collaborative graph learning. *IEEE Transactions on Multimedia*, 22(1):160–173, 2019.
- [73] D. Vázquez, J. Bernal, F. J. Sánchez, G. Fernández-Esparrach, A. M. López, A. Romero, M. Drozdal, and A. Courville. A benchmark for endoluminal scene segmentation of colonoscopy images. *Journal of Healthcare Engineering*, 2017(1):4037190, 2017.
- [74] T. F. Y. Vicente, M. Hoai, and D. Samaras. Leave-one-out kernel optimization for shadow detection. In *Proceedings of IEEE International Conference on Computer Vision*, pages 3388–3396, 2015.
- [75] T. F. Y. Vicente, L. Hou, C.-P. Yu, M. Hoai, and D. Samaras. Large-scale training of shadow detectors with noisily-annotated shadow examples. In *Proceedings of European Conference on Computer Vision*, pages 816–832, 2016.
- [76] J. Wang, X. Li, and J. Yang. Stacked conditional generative adversarial networks for jointly learning shadow detection and shadow removal. In *Proceedings of IEEE Conference on Computer Vision and Pattern Recognition*, pages 1788–1797, 2018.
- [77] L. Wang, H. Lu, Y. Wang, M. Feng, D. Wang, B. Yin, and X. Ruan. Learning to detect salient objects with image-level supervision. In *Proceedings of IEEE Conference on Computer Vision and Pattern Recognition*, pages 136–145, 2017.
- [78] M. Wang, Y. Feng, Y. Tang, T. Zhang, Y. Liang, and C. Lv. Global-local medical sam adaptor based on full adaption. *arXiv preprint arXiv:2409.17486*, 2024.
- [79] X. Wang, W. Wang, Y. Cao, C. Shen, and T. Huang. Images speak in images: A generalist painter for in-context visual learning. In *Proceedings of IEEE Conference on Computer Vision and Pattern Recognition*, pages 6830–6839, 2023.
- [80] X. Wang, X. Zhang, Y. Cao, W. Wang, C. Shen, and T. Huang. Seggpt: Towards segmenting everything in context. In *Proceedings of IEEE International Conference on Computer Vision*, pages 1130–1140, 2023.
- [81] Y. Wang, R. Wang, X. Fan, T. Wang, and X. He. Pixels, regions, and objects: Multiple enhancement for salient object detection. In *Proceedings of IEEE Conference on Computer Vision and Pattern Recognition*, pages 10031–10040, 2023.
- [82] J. Wei, Y. Hu, S. Cui, S. K. Zhou, and Z. Li. Weakpolyp: You only look bounding box for polyp segmentation. In *Proceedings of International Conference on Medical Image Computing and Computer-Assisted Intervention*, pages 757–766, 2023.

- [83] J. Wu, W. Ji, Y. Liu, H. Fu, M. Xu, Y. Xu, and Y. Jin. Medical sam adapter: Adapting segment anything model for medical image segmentation. *arXiv preprint arXiv:2304.12620*, 2023.
- [84] Y. Wu, Y. Liu, L. Zhang, M. Cheng, and B. Ren. EDN: salient object detection via extremely-downsampled network. *IEEE Transactions on Image Processing*, pages 3125–3136, 2022.
- [85] E. Xie, W. Wang, W. Wang, M. Ding, C. Shen, and P. Luo. Segmenting transparent objects in the wild. In *Proceedings of European Conference on Computer Vision*, pages 696–711, 2020.
- [86] H. Xing, S. Gao, Y. Wang, X. Wei, H. Tang, and W. Zhang. Go closer to see better: Camouflaged object detection via object area amplification and figure-ground conversion. *IEEE Transactions on Circuits and Systems for Video Technology*, 33(10):5444–5457, 2023.
- [87] Q. Yan, L. Xu, J. Shi, and J. Jia. Hierarchical saliency detection. In *Proceedings of IEEE Conference on Computer Vision and Pattern Recognition*, pages 1155–1162, 2013.
- [88] C. Yang, L. Zhang, H. Lu, X. Ruan, and M.-H. Yang. Saliency detection via graph-based manifold ranking. In *Proceedings of IEEE Conference on Computer Vision and Pattern Recognition*, pages 3166–3173, 2013.
- [89] H. Yang, T. Wang, X. Hu, and C. Fu. SILT: shadow-aware iterative label tuning for learning to detect shadows from noisy labels. In *Proceedings of IEEE International Conference on Computer Vision*, pages 12641–12652, 2023.
- [90] X. Yuan, G. Cheng, K. Yan, Q. Zeng, and J. Han. Small object detection via coarse-to-fine proposal generation and imitation learning. In *Proceedings of IEEE International Conference on Computer Vision*, pages 6317–6327, 2023.
- [91] J. Zhang, D.-P. Fan, Y. Dai, X. Yu, Y. Zhong, N. Barnes, and L. Shao. Rgb-d saliency detection via cascaded mutual information minimization. In *Proceedings of IEEE International Conference on Computer Vision*, pages 4338–4347, 2021.
- [92] R. Zhang, P. Lai, X. Wan, D. Fan, F. Gao, X. Wu, and G. Li. Lesion-aware dynamic kernel for polyp segmentation. In *Proceedings of International Conference on Medical Image Computing and Computer-Assisted Intervention*, pages 99–109, 2022.
- [93] X. Zhao, H. Jia, Y. Pang, L. Lv, F. Tian, L. Zhang, W. Sun, and H. Lu. M²snet: Multi-scale in multi-scale subtraction network for medical image segmentation. *arXiv preprint arXiv:2303.10894*, 2023.
- [94] X. Zhao, H. Liang, P. Li, G. Sun, D. Zhao, R. Liang, and X. He. Motion-aware memory network for fast video salient object detection. *IEEE Transactions on Image Processing*, 33:709–721, 2024.
- [95] X. Zhao, Y. Pang, Z. Chen, Q. Yu, L. Zhang, H. Liu, J. Zuo, and H. Lu. Towards automatic power battery detection: New challenge benchmark dataset and baseline. In *Proceedings of IEEE Conference on Computer Vision and Pattern Recognition*, pages 22020–22029, 2024.
- [96] X. Zhao, Y. Pang, W. Ji, B. Sheng, J. Zuo, L. Zhang, and H. Lu. Spider: A unified framework for context-dependent concept understanding. In *Proceedings of International Conference on Machine Learning*, pages 60906–60926, 2024.
- [97] X. Zhao, Y. Pang, L. Zhang, H. Lu, and L. Zhang. Towards diverse binary segmentation via a simple yet general gated network. *International Journal of Computer Vision*, 132:4157–4234, 2024.
- [98] X. Zhao, L. Zhang, and H. Lu. Automatic polyp segmentation via multi-scale subtraction network. In *Proceedings of International Conference on Medical Image Computing and Computer-Assisted Intervention*, pages 120–130, 2021.
- [99] T. Zhou, Y. Zhang, Y. Zhou, Y. Wu, and C. Gong. Can sam segment polyps? *arXiv preprint arXiv:2304.07583*, 2023.
- [100] Y. Zou, J. Jeong, L. Pemula, D. Zhang, and O. Dabeer. Spot-the-difference self-supervised pre-training for anomaly detection and segmentation. In *Proceedings of European Conference on Computer Vision*, pages 392–408, 2022.

Table 16: Dataset links.

Task	Dataset Name	Link
Image Salient Object Detection	DUTS	http://saliencydetection.net/duts
Image Salient Object Detection	ECSSD	https://www.cse.cuhk.edu.hk/~leo/jia/projects/hsaliency/dataset.html
Image Salient Object Detection	DUT-OMRON	http://saliencydetection.net/dut-omron
Image Salient Object Detection	HKU-IS	https://arxiv.org/abs/1503.08663
Image Salient Object Detection	PASCAL-S	https://ccvl.jhu.edu/datasets
Video Salient Object Detection	DAVIS16	https://davischallenge.org/davis2016/code.html
Video Salient Object Detection	DAVSOD	https://github.com/DengPingFan/DAVSOD
Image Camouflaged Object Detection	CAMO	https://sites.google.com/view/ltnghia/research/camo
Image Camouflaged Object Detection	COD10K	https://github.com/DengPingFan/SINet
Image Camouflaged Object Detection	NC4K	https://github.com/JingZhang617/COD-Rank-Localize-and-Segment
Video Camouflaged Object Detection	CAD	http://vis-www.cs.umass.edu/motionSegmentation
Video Camouflaged Object Detection	MoCA-Mask	https://github.com/XuelianCheng/SLT-Net
Image Shadow Detection	SBU	https://www3.cs.stonybrook.edu/~cvt/projects/shadow_noisy_label
Image Shadow Detection	ISTD	https://github.com/DeepInsight-PCALab/ST-CGAN
Video Shadow Detection	VISAD	https://github.com/yihong-97/STICT
Transparent Object Segmentation	Trans10K	https://xieenze.github.io/projects/TransLAB/TransLAB.html
Image Polyp Lesion Segmentation	Kvasir	https://datasets.simula.no/kvasir-seg
Image Polyp Lesion Segmentation	ETIS	https://polyp.grand-challenge.org/ETISLarib
Image Polyp Lesion Segmentation	CVC-ClinicDB	https://polyp.grand-challenge.org/CVCClinicDB
Image Polyp Lesion Segmentation	CVC-ColonDB	http://vi.cvc.uab.es/colon-qa/cvccolondb
Image Polyp Lesion Segmentation	Endoscene	https://arxiv.org/abs/1612.00799
Video Polyp Lesion Segmentation	Video Polyp	https://github.com/GewelsJI/PMS-Net
Skin Lesion Segmentation	ISIC-2018	https://challenge.isic-archive.com/landing/2018
COVID-19 Lung Infection Segmentation	COVID-19 CT	https://github.com/DengPingFan/Inf-Net
Brain Tumor Segmentation	BraTS2020	https://www.med.upenn.edu/cbica/brats2020
Brain Tumor Segmentation	ISBI2015	https://smart-stats-tools.org/lesion-challenge-2015
Breast Lesion Segmentation	BUSI	https://scholar.cu.edu.eg/?q=afahmy/pages/dataset
Power Battery Detection	X-ray PBD	https://github.com/Xiaoqi-Zhao-DLUT/X-ray-PBD
Surface Anomaly Detection	MVTec-AD	https://www.mvtec.com/company/research/datasets/mvtec
Surface Anomaly Detection	VisA	https://github.com/amazon-science/spot-diff
Surface Anomaly Detection	BTAD	https://ieeexplore.ieee.org/abstract/document/9576231

Appendix

A Datasets

A.1 Natural Scene Data

Image Salient Object Detection. DUTS [77] consists of 10,553 training images and 5,019 testing images, covering diverse scenes with high-quality pixel-level saliency annotations and widely used for evaluating salient object detection models. ECSSD [87] includes 1,000 images containing complex scenes where salient objects often blend into the background, challenging models to differentiate salient regions. DUT-OMRON [88] features 5,168 images with complex backgrounds and small objects, making it an essential dataset for assessing the robustness of salient object detection algorithms. HKU-IS [40] contains 4,447 images (2500 for training, 500 for validation, and 1447 for testing) with detailed edge annotations, focusing on large salient objects with clear boundaries, which challenge models to capture fine-grained details. PASCAL-S [41] is derived from PASCAL VOC 2010 with 850 images annotated by multiple experts, aiming to test saliency models in natural and complex scenes. In our experiments, the data for testing is from ECSSD, DUT-OMRON, PASCAL-S, and the testing sets of DUTS and HKU-IS.

Video Salient Object Detection. DAVIS16 [57] is a benchmark dataset comprising 50 high-quality video sequences (30 for training and 20 for validation) with pixel-level annotations for object segmentation in dynamic scenes. The dataset is characterized by complex settings, including frequent occlusions, fast motion, and intricate backgrounds, making it a popular choice for evaluating video object segmentation models. In our experiments, we use the validation subset of DAVIS16, which contains 20 sequences specifically selected to assess the generalization performance of models in diverse and challenging scenarios. DAVSOD [25] is a large-scale video saliency detection dataset that includes 226 video sequences (61 for training, 46 for validation, and 80 for testing) with pixel-level saliency annotations. It is designed to evaluate models in a wide range of scenarios, including dynamic scenes and camouflaged objects, providing a comprehensive benchmark for saliency detection tasks. The testing set is divided into three splits based on difficulty levels: DAVSOD_E (easy, 35 sequences), DAVSOD_N (normal, 25 sequences), and DAVSOD_H (hard, 20 sequences). These splits allow for a nuanced evaluation of model performance under varying complexities, ranging from relatively straightforward scenes to highly intricate and visually challenging scenarios. In our study, we use

all three splits to comprehensively analyze the model’s robustness and adaptability across different difficulty levels.

Image Camouflaged Object Detection. Following the recent typical methods [56, 86], we adopt a similar evaluation strategy for the CAMO [39], COD10K [22], and NC4K [51] datasets. Specifically, for CAMO, we use a subset containing 1,250 images that include camouflaged objects. CAMO is a specialized dataset designed to evaluate the detection of camouflaged objects in complex backgrounds, featuring a diverse range of challenging scenarios where objects are intentionally concealed within their surroundings. For COD10K, we focus on a subset of 5,066 images that are carefully selected to include scenes with camouflaged objects. This subset is annotated with pixel-level ground truth, providing a comprehensive benchmark for evaluating model performance in detecting objects that seamlessly blend into diverse and complex natural environments. For NC4K, we use the entire dataset comprising 4,121 high-resolution images. NC4K is specifically curated to assess model generalization capabilities by presenting camouflaged objects across a wide variety of natural scenes with intricate details and challenging visual conditions. Notably, in our experiments, we follow the common practice of only testing on images containing camouflaged objects for CAMO and COD10K, while using the entire NC4K dataset as the test set. This evaluation protocol ensures consistency with recent works and provides a fair comparison of model performance.

Video Camouflaged Object Detection. CAD [5], consisting of 9 sequences, focuses on camouflaged object detection in continuous video frames, emphasizing the temporal consistency of models in dynamic backgrounds. MoCA-Mask [14] features high-quality mask annotations for camouflaged objects in videos, challenging models to detect and segment targets in motion. It is divided into two subsets: 71 sequences for training and 16 sequences for testing. The entire CAD dataset and the testing subset of MoCA-Mask are used for evaluating the methods.

Image Shadow Detection. SBU [75] is a widely-used benchmark dataset for shadow detection. Its testing set contains 700 outdoor scene images with pixel-level shadow annotations. These images include diverse scenarios with shadows cast by various objects, providing a robust basis for evaluating the precision of shadow detection models. ISTD [76] contains 1,870 sets of images, each consisting of a shadow image, a shadow-free counterpart, and a shadow mask. This dataset is specifically designed for both shadow detection and removal tasks. It is randomly split into 1,330 image sets for training and 540 image sets for testing. In our experiments, we directly use the testing sets of both SBU and ISTD, ensuring consistency with prior works.

Video Shadow Detection. VISAD [48] is a comprehensive video shadow detection dataset comprising 81 videos, curated from various public video datasets to address the challenges of detecting shadows in dynamic scenarios. The dataset is divided into two subsets based on scene types: the Driving Scenes (VISAD-DS) subset and the Moving Object Scenes (VISAD-MOS) subset, denoted as DS and MOS, respectively. This division enables targeted evaluation of shadow detection models across distinct real-world settings. VISAD-DS focuses on driving scenarios, featuring videos captured in urban streets, highways, and similar environments. Shadows in this subset are typically caused by moving vehicles, pedestrians, and static objects such as buildings and trees. The interplay of dynamic elements and structured backgrounds makes this subset a challenging benchmark, particularly for detecting shadows that may overlap with objects of interest or blend with road features. VISAD-MOS highlights scenes dominated by moving objects, such as people, animals, or vehicles, in more diverse and unstructured environments. Shadows in these videos are influenced by variable lighting conditions and intricate object interactions, making it a critical test bed for evaluating models’ ability to generalize across complex scenarios. By utilizing both VISAD-DS and VISAD-MOS in our experiments, we aim to comprehensively evaluate the performance of shadow detection models across a wide spectrum of dynamic and challenging settings. This approach ensures a robust assessment of models’ adaptability to diverse scene characteristics.

Transparent Object Segmentation. Trans10K [85] contains 10,428 images designed for pixel-level segmentation of transparent objects, which are challenging due to their translucent nature.

A.2 Medical Scene Data

Image Polyp Lesion Segmentation. There are five popular polyp segmentation datasets. Kvasir [31] contains 1,000 colonoscopy polyp images. ETIS [66] with 196 high-resolution images focus on detecting small polyps. CVC-ClinicDB [4] with 612 colonoscopy images commonly used for

segmentation evaluation. CVC-ColonDB [69] comprising 380 images with complex backgrounds challenging models to detect small objects, and Endoscene [73] with 912 images covering diverse polyp detection scenarios. Since these datasets are small in data-scale, in order to avoid performance volatility as much as possible, we follow the Spider [96] to calculate the average results of the five datasets for performance evaluation.

Video Polyp Lesion Segmentation. CVC-612-T [32], CVC-612-V [32], and CVC-300-TV [32] focus on polyp segmentation in video sequences, considering temporal continuity and dynamic information.

Skin Lesion Segmentation. ISIC-2018 [16] is the ISIC challenge dataset containing over 13,000 skin lesion images with detailed segmentation annotations, primarily for melanoma detection.

COVID-19 Lung Infection Segmentation. COVID-19 CT [26] comprises CT scans of COVID-19 patients with pixel-level annotations for lung infection areas.

Brain Tumor Segmentation. BraTS2020 [54] is an MRI-based dataset focused on brain tumor segmentation, providing detailed multi-modal annotations, including T1, T2, T1ce, and Flair sequences, to capture various tumor structures. ISBI2015 [8] is a dataset for multiple sclerosis lesion segmentation, from which we specifically utilize the Flair modality to detect and analyze lesion areas.

Breast Lesion Segmentation. BUSI [1] is an ultrasound dataset containing pixel-level annotations for breast lesions, widely used in breast cancer detection research.

A.3 Industrial Scene Data

Power Battery Detection. PBD [95] is an X-ray dataset used for detecting defects in power batteries, particularly focusing on internal structural issues.

Surface Anomaly Detection. MVTec-AD [3] includes high-resolution images across 15 categories of industrial products used for detecting surface defects. VisA [100] covers various industrial products for visual anomaly detection, focusing on defect detection across different materials. BTAD [55] contains ultra-high-resolution images for detecting small defects on metal surfaces.

B Evaluation Metrics

For salient object detection (SOD) and camouflaged object detection (COD), we utilize weighted F-measure (F_{β}^w) [53], S-measure (S_m) [20], and mean absolute error (MAE). The weighted F-measure accounts for spatial significance by assigning greater weight to pixels in critical regions, thereby providing a more precise balance between precision and recall. The S-measure emphasizes structural similarity between the predicted saliency map and the ground truth, combining object-aware and region-aware evaluations to capture holistic accuracy. Meanwhile, the MAE serves as a straightforward metric to calculate the pixel-wise average absolute difference, offering an intuitive measure of overall prediction accuracy without considering spatial structure.

For shadow detection (SD) and transparent object segmentation (TOS), where significant class imbalance often exists, we adopt the balanced error rate (BER) [74]. This metric is defined as the average of the false positive rate (FPR) and false negative rate (FNR), ensuring that the evaluation remains fair across imbalanced datasets by equally penalizing errors in both positive and negative classes.

In medical lesion object segmentation (LOS), where precise mask overlap is critical, intersection over union (IoU) and the Dice similarity coefficient are employed. The metric IoU quantifies the ratio of the overlap between predicted and ground-truth masks to their union, providing a robust measure of segmentation accuracy. The Dice coefficient complements IoU by focusing on the similarity of the overlapping regions while penalizing false positives and false negatives, making it particularly effective for medical image analysis tasks.

For power battery detection (PBD), both spatial accuracy and numerical correctness are of primary importance. Location mean absolute error (AL-MAE, CL-MAE, OH-MAE) [95] evaluates the mean absolute error of detected locations under different configurations, such as alignment, clustering, and outlier handling. Additionally, point number accuracy (PN-ACC) measures the ability to predict the

correct number of detected power battery units, ensuring reliability in industrial applications where both detection precision and count accuracy are essential.

In the domain of surface anomaly detection (AD), a combination of image-level and pixel-level metrics is utilized. At the image level, we employ I-AUROC and I-AP to assess overall classification performance, with the former measuring the area under the receiver operating characteristic curve and the latter summarizing precision-recall tradeoffs. At the pixel level, P-AUROC and P-AP provide analogous measures for segmentation performance, focusing on the accurate localization of anomalous regions. Additionally, P-PRO quantifies the per-region overlap between predicted and ground-truth anomalous regions, offering a fine-grained evaluation of segmentation quality that emphasizes spatial alignment.

These metrics collectively provide a comprehensive framework for evaluating model performance across diverse tasks, addressing challenges such as class imbalance, structural similarity, spatial alignment, and numerical accuracy. By leveraging these tailored evaluation measures, we ensure a rigorous and fair assessment of the SAMs under various application scenarios. The implementation of all evaluation metrics is based on the publicly available toolkits.²

C Prediction Generation

C.1 Basic Mode

Point Prompt (⊙). To mimic this pattern of interaction, we design automated processes that simulate successive clicking behaviors. Each step clicks on the position farthest from the background selected from the FP and FN regions in the prediction. Finally, the prediction mask is generated through an iterative process of adding clicks to improve mask prediction until a maximum IoU threshold (0.9) is reached or a limit on the number of clicks (6) is hit.

Box Prompt (⌊⋮). The process involves generating a final prediction through a series of steps: First, all bounding boxes are obtained for connected regions within the ground truth mask (GT). Next, multiple masks are predicted using these bounding boxes. Finally, the final prediction is constructed by performing a logical OR operation across all individual masks, resulting in a union of all predicted masks.

Mask Prompt (✎). For images, directly using the original mask as a prompt does not hold practical value. However, for video tasks, the setup of using a mask as the prompt has been extensively explored in some context-independent concept understanding tasks like one-shot video object segmentation. Therefore, in this work, it is only utilized in video data on specific reference frames. And the performance of SAM 2 under this setup is tested exclusively.

Automatic Generation (⊞). In interaction-based types including points (⊙), bounding boxes (⌊⋮), and masks (✎), we can directly obtain the final predictions through SAM or SAM 2. However, the output in the automatic type is a segmentation map containing all local entities in the entire image, which cannot be directly used in the performance evaluation for these tasks. Therefore, the *overlap filtering strategy (OFS)* based on the ground-truth mask (GT) is employed here, retaining only those independent entities whose overlap area with the GT is greater than 90%. These retained entities are merged into a mask, serving as the final prediction result.

C.2 In-Context Learning Mode

As detailed in Sec. 3.3, the memory mechanism in SAM 2 enables implicit modeling of contextual knowledge. To investigate this capability, we evaluate its performance under the In-Context Learning (ICL) mode. In this mode, SAM 2 does not rely solely on prompts from the current image. Instead, it incorporates multiple concept exemplars to pre-encode and interpret diverse semantic representations. This approach facilitates more precise segmentation and robust modeling of scene elements, particularly in context-dependent (CD) tasks. Unlike traditional methods, which are constrained to single-image information, the ICL mode enhances SAM 2’s understanding ability by utilizing

²https://github.com/Xiaoqi-Zhao-DLUT/PySegMetric_EvalToolkit
https://github.com/zaoyuan1209/PyADMetric_EvalToolkit
<https://github.com/Xiaoqi-Zhao-DLUT/X-ray-PBD>

additional contextual information from a set of 20 training images and their corresponding masks. For generality, these 20 images are directly chosen as the first 20 samples in the training dataset. These exemplar samples enrich the contextual representation, offering substantial benefits for comprehending CD concepts.

C.3 Bidirectional Inference for 3D data

Some 3D medical lesion image sequences typically begin and end with slices consisting of pure background and no discernible foreground objects. In such cases, prompting SAM 2 with a pure background frame may lead to unreasonable results. To address this challenge, we evaluate the performance of SAM 2 using our proposed bidirectional inference strategy. First, we traverse the entire 3D sequence to identify the slice with the largest foreground region, which serves as the anchor point for the process. The sequence is then split into two subsequences: the first subsequence spans from the beginning of the sequence to the anchor slice, and the second subsequence spans from the anchor slice to the end. Starting from the anchor slice, SAM 2 performs bidirectional inference by propagating segmentation masks in opposite directions: one direction traverses forward through the second subsequence toward the end of the sequence, while the other direction traverses backward through the first subsequence toward the start of the sequence. This dual traversal ensures that segmentation information is propagated effectively across all slices, leveraging both spatial context and temporal consistency. After completing inference in both directions, the results are combined to form the final prediction for the entire 3D sequence. This strategy improves segmentation accuracy by enhancing continuity across slices and mitigating the impact of slices with purely background information, ultimately enabling more reliable and consistent segmentation results for 3D medical image sequences.

C.4 Visualization

Fig. 6, 7, 8, 9, 10, 11, 12, 13, 14, 15, 16, 17 show the visualization results of SAM and SAM 2 on various context-dependent (CD) concepts.

D Details of Robustness Analysis

D.1 Random Perturbation for Point Mode (⊙)

Expanding on the multi-click strategy described in the point prompt of Sec. C.1, we propose a perturbation method that randomly shifts the horizontal and vertical coordinates of each point by up to 10 pixels. These random offsets introduce variations in the point placements, enabling us to evaluate the model’s performance when the spatial configuration of point prompts is slightly altered. This method provides insight into the model’s robustness against coordinate distortions and uncertainties in point-based inputs.

D.2 Random Perturbation for Box Mode (☐)

Building upon the method described in the box prompt of Sec. C.1, we propose a strategy to perturb bounding boxes by introducing random errors to enhance robustness against annotation noise and spatial uncertainties. The perturbation adjusts each boundary within a maximum range of 10% of the shorter side of the bounding box, ensuring proportional adaptability to varying object scales. To maintain validity, the perturbed boxes are constrained to remain within the image boundaries. This approach effectively simulates real-world imperfections, providing a more resilient foundation for model training and evaluation.

D.3 Random Perturbation for Mask Mode (👤)

To assess the robustness of the model under the mask prompt strategy described in the mask prompt of Sec. C.1, we introduce a method that applies random morphological transformations to the input mask. Specifically, the binary mask is randomly subjected to either erosion or dilation, with the number of iterations varying up to a maximum of 5. This controlled perturbation introduces variations in the mask’s boundaries and structure, enabling a comprehensive evaluation of the model’s ability to handle spatial distortions and inconsistencies in mask prompts.

D.4 Random Perturbation on Video Data

For video data, SAM uses an image-based prompting approach, whereas for SAM 2, we focus on the setting of a single prompt.

D.5 Relative Performance Change Δ

Due to the established inheritance relationship, the average performance after perturbation, as shown in Tab. 15, can be compared with the ideal prompt performance based on ground truth listed in Tab. 2, 7, 11. So we can obtain the relative performance change Δ in Tab. 15.

E Why the Context-Dependent (CD) Concepts are Important for SAM?

1) Research Value of CD Concepts Themselves. CD concepts, such as visual saliency, visual camouflage, medical lesions, and industrial defects, have long-standing research and practical value. Segmenting and understanding these CD concepts have garnered significant attention both in academic conferences and real-world applications. For example, in medical imaging (*e.g.*, brain or colon lesion segmentation), these tasks are critical for advancing human health. Similarly, in industrial quality assessment (*e.g.*, lithium battery electrode or surface defect segmentation), they play a vital role in ensuring safety and reliability.

2) Motivation of Evaluating SAMs. As the foundational segmentation models, SAM and SAM 2 (SAMs) aim to handle diverse segmentation tasks. However, the original paper primarily evaluated its performance on context-dependent (CI) datasets. A comprehensive evaluation of SAMs on CD concepts helps the community accurately understand the performance boundaries of SAMs. We believe this will hold significant value for future applications and model upgrades.

3) Directions for Improving SAMs. By analyzing SAMs' strengths and weaknesses on CD concepts and comparing them with other unified models, we can provide meaningful outlooks for the next generation of SAM.

F Limitations

We outline improvement suggestions in Sec. 4, summarizing characteristics of unified segmentation models. While full implementation would require dedicated research (potentially spanning multiple studies), such engineering efforts including novel module architectures and large-scale dataset curation, exceed the scope of this evaluation-focused work. Evaluating the feasibility of these outlook suggestions and implementing them will require collaborative efforts from the broader research community.

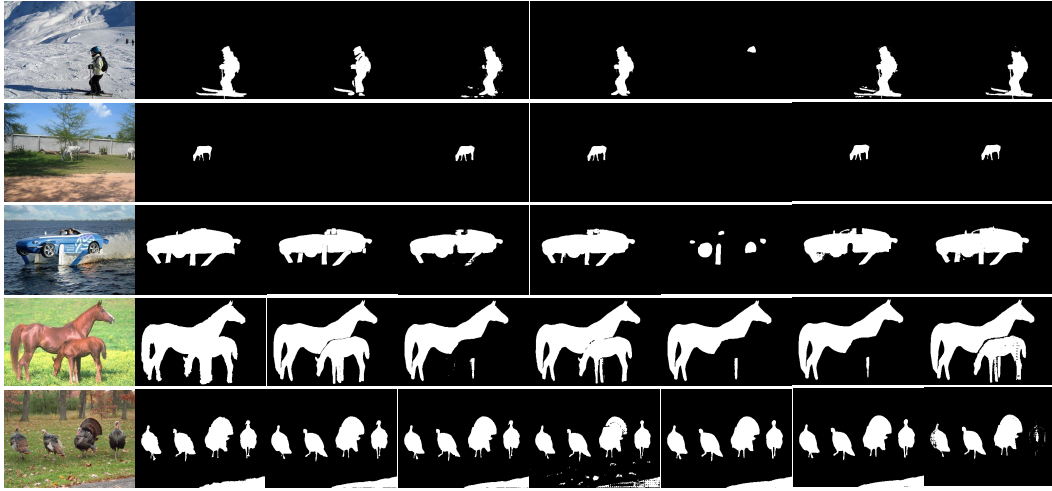


Figure 6: Visualization of salient object detection. From left to right: Image, Ground Truth, SAM (⊞), SAM (⊞), SAM (⊙), SAM 2 (⊞), SAM 2 (⊞), SAM 2 (⊙).

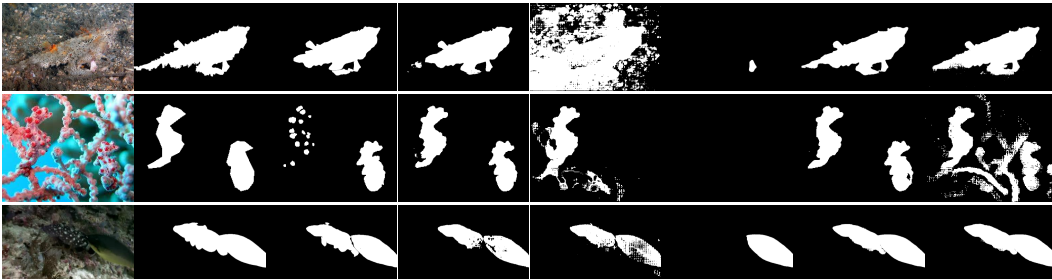


Figure 7: Visualization of camouflaged object detection. From left to right: Image, Ground Truth, SAM (⊞), SAM (⊞), SAM (⊙), SAM 2 (⊞), SAM 2 (⊞), SAM 2 (⊙).

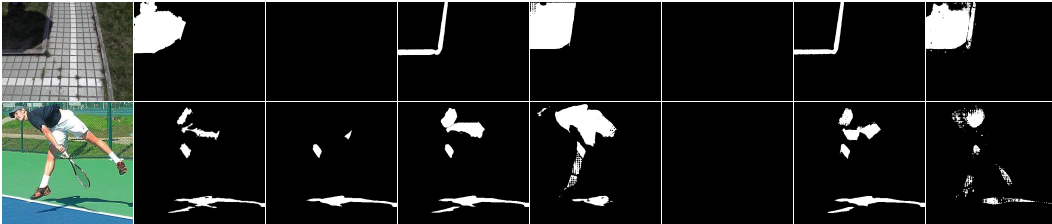


Figure 8: Visualization of shadow detection. From left to right: Image, Ground Truth, SAM (⊞), SAM (⊞), SAM (⊙), SAM 2 (⊞), SAM 2 (⊞), SAM 2 (⊙).



Figure 9: Visualization of transparent object segmentation. From left to right: Image, Ground Truth, SAM (⊞), SAM (⊞), SAM (⊙), SAM 2 (⊞), SAM 2 (⊞), SAM 2 (⊙).



Figure 10: Visualization of power battery detection. From left to right: Image, Ground Truth, SAM (⊞), SAM (⋮), SAM (⊙), SAM 2 (⊞), SAM 2 (⋮), SAM 2 (⊙).

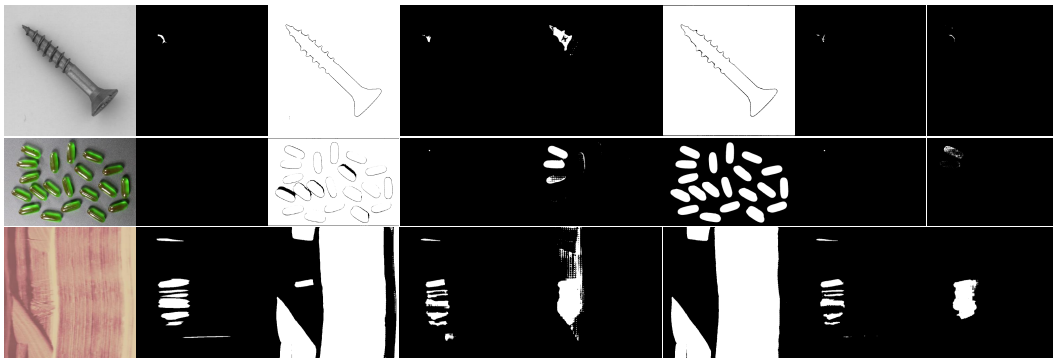


Figure 11: Visualization of surface anomaly detection. From left to right: Image, Ground Truth, SAM (⊞), SAM (⋮), SAM (⊙), SAM 2 (⊞), SAM 2 (⋮), SAM 2 (⊙).

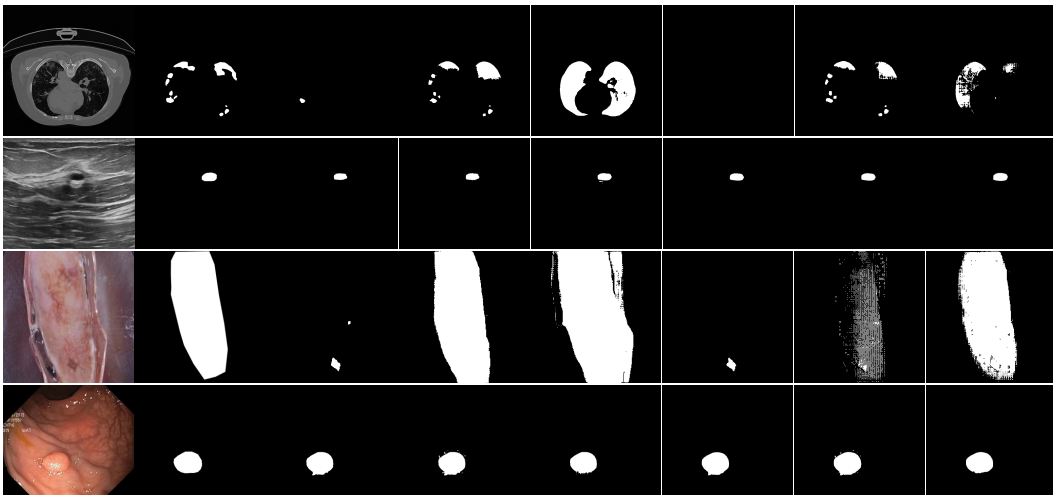


Figure 12: Visualization of medical lesion segmentation (Lung, Breast, Skin, Polyp). From left to right: Image, Ground Truth, SAM (⊞), SAM (⋮), SAM (⊙), SAM 2 (⊞), SAM 2 (⋮), SAM 2 (⊙).



Figure 13: Visualization of video polyp segmentation. From top to bottom: Image, Ground Truth, SAM (⊞), SAM (⊠), SAM (Propagated ⊠), SAM (⊙), SAM (Propagated ⊙), SAM 2 (1×⊠), SAM 2 (3×⊠), SAM 2 (5×⊠), SAM 2 (1×⊕), SAM 2 (3×⊕), SAM 2 (5×⊕), SAM 2 (1×⊙), SAM 2 (3×⊙), SAM 2 (5×⊙).

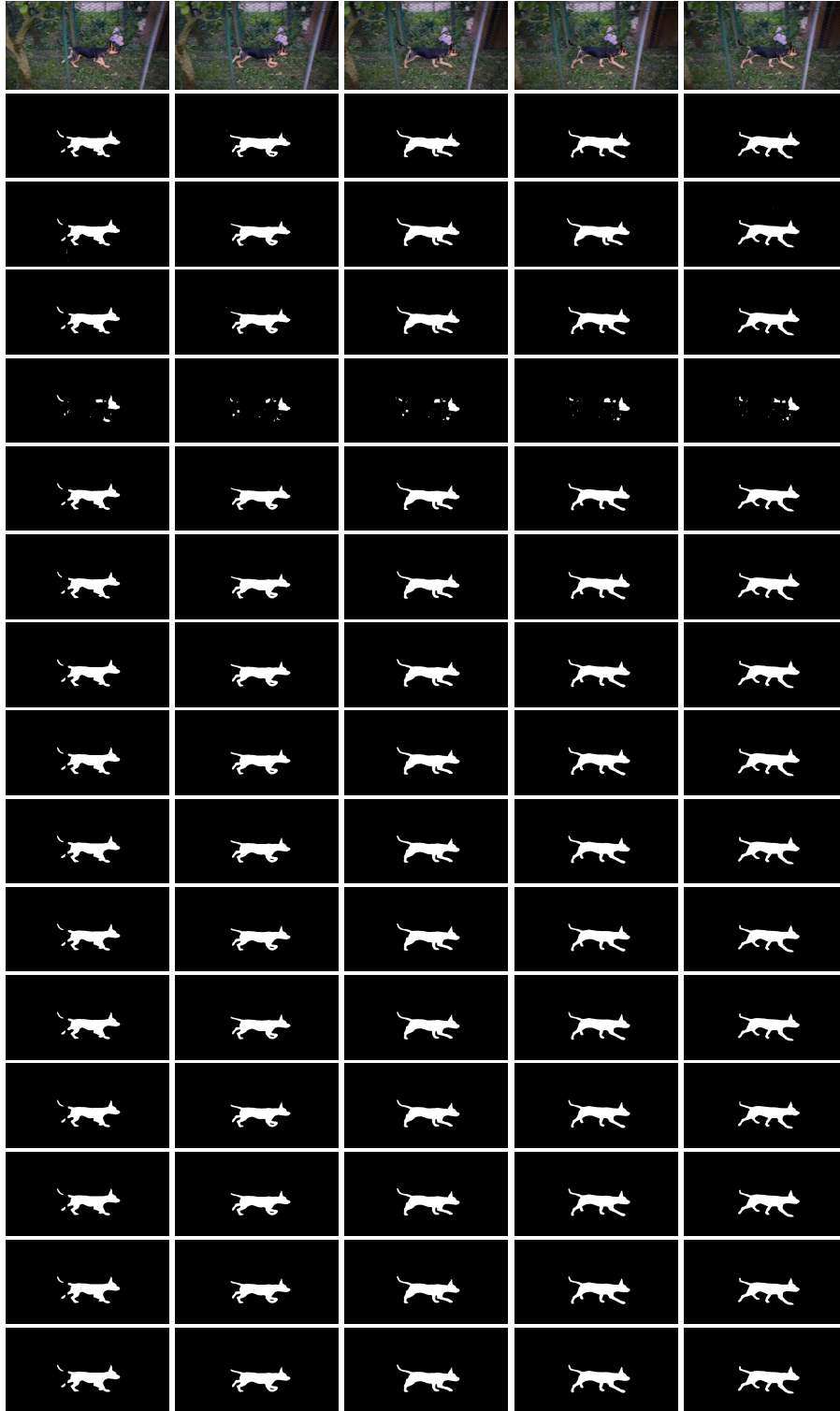


Figure 14: Visualization of video salient object detection. From top to bottom: Image, Ground Truth, SAM (⊞), SAM (⊞), SAM (Propagated ⊞), SAM (⊙), SAM (Propagated ⊙), SAM 2 (1×⊞), SAM 2 (3×⊞), SAM 2 (5×⊞), SAM 2 (1×⊞), SAM 2 (3×⊞), SAM 2 (5×⊞), SAM 2 (1×⊙), SAM 2 (3×⊙), SAM 2 (5×⊙).

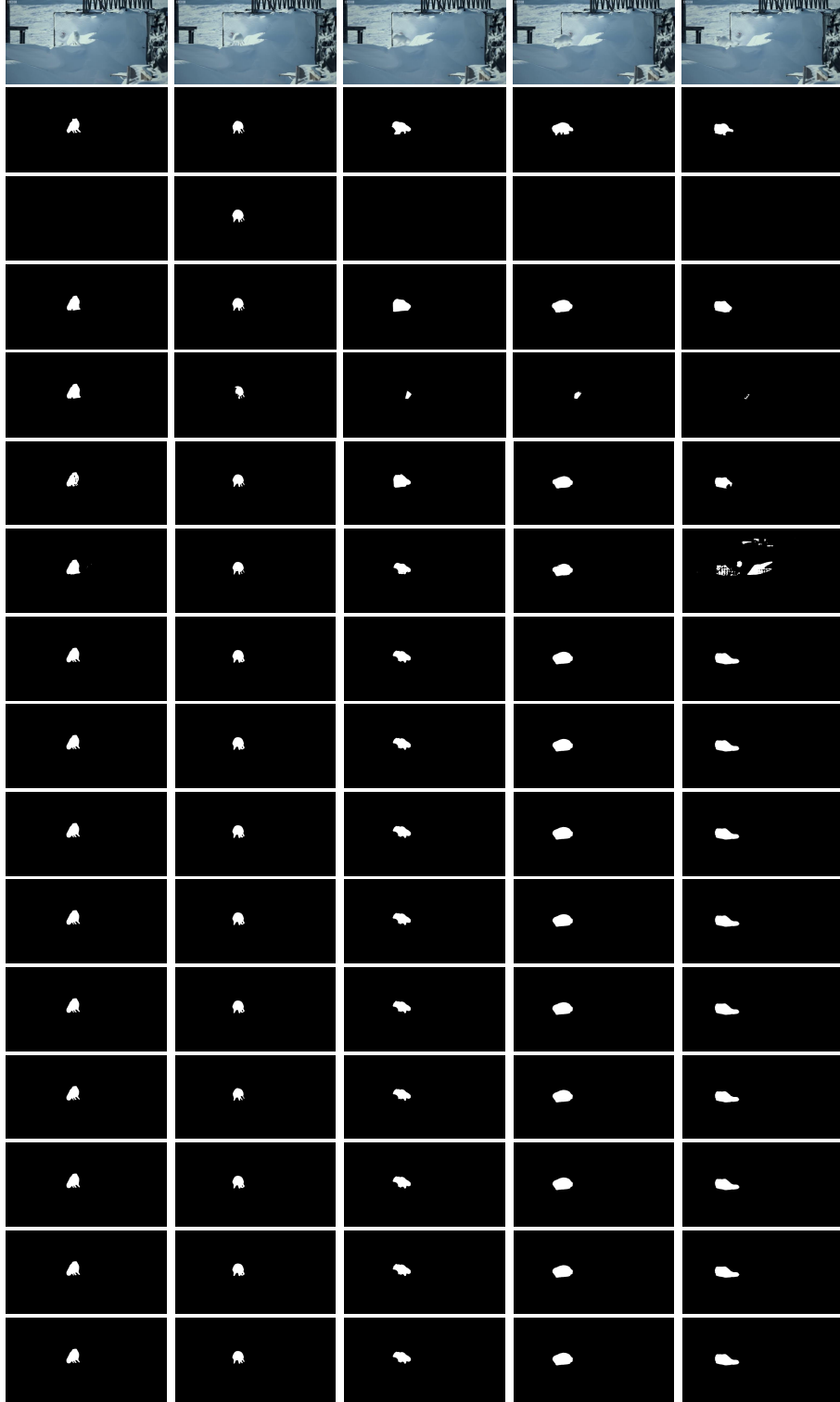


Figure 15: Visualization of video camouflaged object detection. From top to bottom: Image, Ground Truth, SAM (grid), SAM (dots), SAM (Propagated dots), SAM (circle), SAM (Propagated circle), SAM 2 (1x dots), SAM 2 (3x dots), SAM 2 (5x dots), SAM 2 (1x star), SAM 2 (3x star), SAM 2 (5x star), SAM 2 (1x circle), SAM 2 (3x circle), SAM 2 (5x circle).

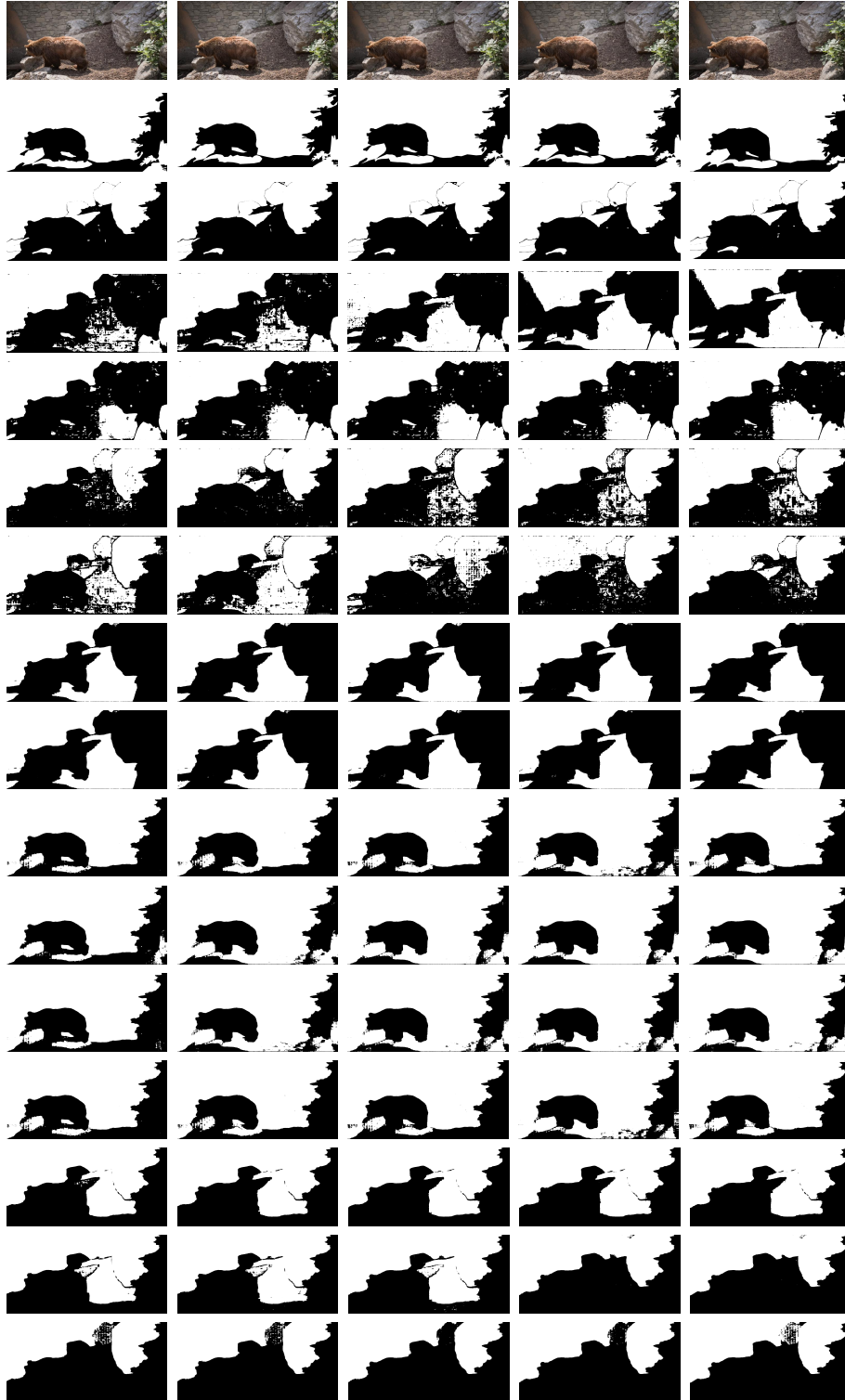


Figure 16: Visualization of video shadow detection. From top to bottom: Image, Ground Truth, SAM (⊕), SAM (⊖), SAM (Propagated ⊖), SAM (⊙), SAM (Propagated ⊙), SAM 2 (1×⊖), SAM 2 (3×⊖), SAM 2 (5×⊖), SAM 2 (1×⊕), SAM 2 (3×⊕), SAM 2 (5×⊕), SAM 2 (1×⊙), SAM 2 (3×⊙), SAM 2 (5×⊙).

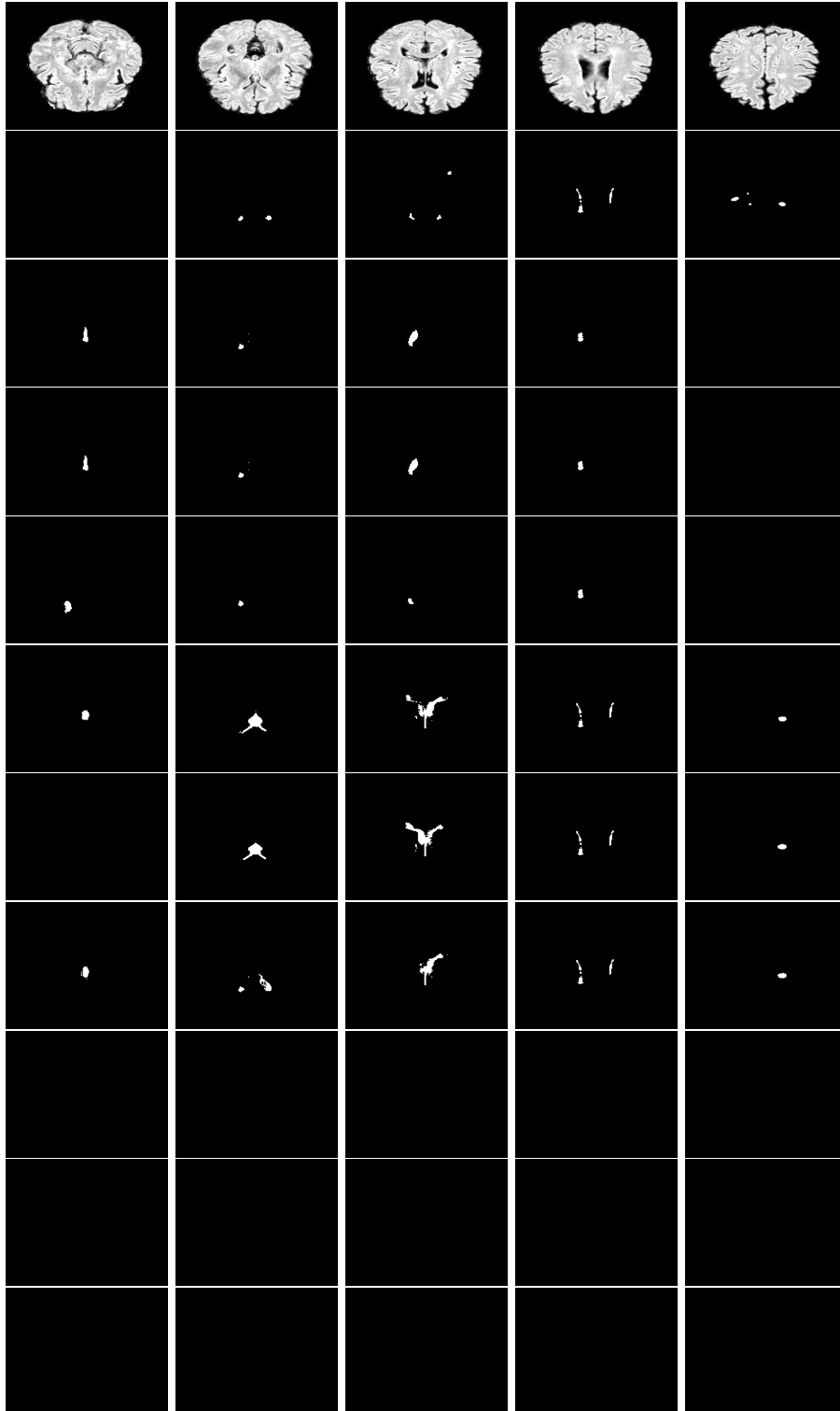


Figure 17: Visualization of 3D brain tumor segmentation. From top to bottom: Image, Ground Truth, SAM 2 (1× \square), SAM 2 (3× \square), SAM 2 (5× \square), SAM 2 (1× \star), SAM 2 (3× \star), SAM 2 (5× \star), SAM 2 (1× \odot), SAM 2 (3× \odot), SAM 2 (5× \odot).